Atmos. Chem. Phys., 23, 13191–13215, 2023
https://doi.org/10.5194/acp-23-13191-2023

Atmospheric Chemistry and Physics
Open Access
EGU

Numerical simulation and evaluation of global ultrafine particle concentrations at the Earth's surface

Matthias Kohl[1], Jos Lelieveld[1,2], Sourangsu Chowdhury[3], Sebastian Ehrhart[4], Disha Sharma[1], Yafang Cheng[5], Sachchida Nand Tripathi[6], Mathew Sebastian[7], Govindan Pandithurai[8], Hongli Wang[9], and Andrea Pozzer[1,2]

[1]Atmospheric Chemistry Department, Max Planck Institute for Chemistry, Mainz, Germany
[2]Climate and Atmosphere Research Center, The Cyprus Institute, Nicosia, Cyprus
[3]CICERO Center for International Climate Research, Oslo, Norway
[4]Finnish Environment Institute (SYKE), Marine Research Centre, Helsinki, Finland
[5]Minerva Research Group, Max Planck Institute for Chemistry, Mainz, Germany
[6]Department of Civil Engineering, Indian Institute of Technology Kanpur, Kanpur, India
[7]Centre for Earth, Ocean and Atmospheric Sciences, University of Hyderabad, Hyderabad, India
[8]Indian Institute of Tropical Meteorology, Ministry of Earth Sciences, Pune, India
[9]State Environmental Protection Key Laboratory of Formation and Prevention of Urban Air Pollution Complex, Shanghai Academy of Environmental Sciences, Shanghai 200233, China

Correspondence: Matthias Kohl (m.kohl@mpic.de) and Andrea Pozzer (andrea.pozzer@mpic.de)

Received: 21 February 2023 – Discussion started: 28 February 2023
Revised: 7 September 2023 – Accepted: 11 September 2023 – Published: 19 October 2023

Abstract. A new global dataset of annually averaged ultrafine particle (UFP) concentrations at the Earth's surface for the years 2015–2017 has been developed through numerical simulations using the ECHAM/MESSy Atmospheric Chemistry model (EMAC). We present total and size-resolved concentrations along with their inter-annual variability. Size distributions of emitted particles from the contributing source sectors have been derived based on literature reports. The model results of UFP concentrations are evaluated using particle size distribution and particle number concentration measurements from available datasets and the literature. While we obtain reasonable agreement between the model results and observations (logarithmic-scale correlation of $r = 0.76$ for non-remote, polluted regions), the highest values of observed, street-level UFP concentrations are systematically underestimated, whereas in rural environments close to urban areas the model generally overestimates observed UFP concentrations. As the relatively coarse global model does not resolve concentration gradients in urban centres and industrial UFP hotspots, high-resolution data of anthropogenic emissions are used to account for such differences in each model grid box, obtaining UFP concentrations with unprecedented $0.1° \times 0.1°$ horizontal resolution at the Earth's surface. This observation-guided downscaling further improves the agreement with observations, leading to an increase in the logarithmic-scale correlation between observed and simulated UFP concentrations to $r = 0.84$ in polluted environments (and 0.95 in all regions), a decrease in the root mean squared logarithmic error (from 0.57 to 0.43), and removal of discrepancies associated with air quality and population density gradients within the model grid boxes. The model results are made publicly available for studies on public health and other impacts of atmospheric UFPs, as well as for intercomparison with other regional and global models and datasets.

1 Introduction

Atmospheric aerosols in various size ranges have a significant impact on public health, the hydrological cycle and climate. Close to the Earth's surface, aerosol particles are among the main pollutants and drivers of atmospheric chemistry in the boundary layer, being directly relevant for human health (Burnett et al., 2014; Pope and Dockery, 2006; Cohen et al., 2005). At the same time, aerosols can directly scatter and absorb solar and thermal radiation, altering the radiative balance of the Earth's atmosphere (e.g. Bellouin et al., 2020). Furthermore, atmospheric aerosols act as cloud condensation nuclei (CCN) and thus influence cloud formation processes and cloud properties. Consequently, changes in CCN concentrations may affect the hydrological cycle and indirectly the radiative balance of the Earth's atmosphere by altering cloud cover and albedo (e.g. Christensen et al., 2020; Lohmann and Feichter, 2005; Twomey, 1959).

Recently, multiple studies have concluded that the exposure to particulate matter air pollution from a variety of sources has major implications for public health (Lelieveld et al., 2020, 2015; Chowdhury et al., 2022). The latest Global Burden of Disease study has associated 4.2 million deaths globally with the exposure to ambient particulate matter with an aerodynamic diameter smaller than 2.5 µm ($PM_{2.5}$) and 0.37 million deaths to ambient ozone pollution (Murray et al., 2020). Evidence presented in recent studies indicates that the long-time exposure to high concentrations of ultrafine particles (UFPs), i.e. particles with an aerodynamic diameter smaller than 100 nm (WHO, 2006) which barely contribute to $PM_{2.5}$ mass, significantly impacts human health, leading to the increased incidence of cardiovascular and cerebrovascular diseases (Downward et al., 2018; Delfino et al., 2005; Stone et al., 2017). The health impacts of UFPs may be attributed to their high potential to penetrate more deeply into the lungs and potentially into the bloodstream compared to coarser size particles (Schraufnagel et al., 2019; Schraufnagel, 2020; Hong and Jee, 2020).

Reflection and absorption of solar radiation can be neglected for UFPs as the scattering and absorption coefficients typically peak at particle diameters between 400 and 1000 nm. However, aerosol particles with a minimum diameter of approximately 40 nm and larger can serve as CCN, while particle numbers strongly decrease for sizes greater than 200–300 nm in general (Andreae, 2009). Thus, UFPs significantly contribute to CCN concentrations.

Atmospheric aerosols can either be directly emitted into the atmosphere (primary) by natural or anthropogenic processes or be nucleated from precursor gases (secondary), with the latter being considered to be the largest source of atmospheric aerosols (Gordon et al., 2017). Freshly nucleated secondary particles usually have a diameter between 1 and 20 nm (Curtius, 2006) and can grow by coagulation and condensation of trace gases (Kulmala et al., 2004). While primary aerosols from natural sources (e.g. desert dust and sea salt) are emitted at diameters predominantly in the micrometre range and larger (Dentener et al., 2006), anthropogenic particles (e.g. from combustion processes) are usually emitted at much smaller sizes, contributing to UFPs (Kwon et al., 2020; Paasonen et al., 2016).

Despite the importance of UFPs for atmospheric processes and human health, very little is known about their global distribution at the Earth's surface. A simulation of global particle number concentrations at the Earth's surface was performed by Gordon et al. (2017), however focusing on new particle formation (NPF) and CCN up to an altitude of 460 m above the surface, and by Chen et al. (2021) with a nested high-resolution simulation over eastern Asia ($0.33° \times 0.33°$) and a particular focus on organic aerosols. Local (surface or vertical) distributions of particle number concentrations and size distributions were measured and modelled by Ketzel et al. (2021) and Frohn et al. (2021, both street- and address-level UFP concentrations in Denmark), Fountoukis et al. (2012) and Saha et al. (2021, high-resolution UFP concentrations over Europe and the United States, respectively), Kukkonen et al. (2016, dispersion of particle numbers in European cities), Franco et al. (2022, NPF and growth in the Amazon rainforest), Williamson et al. (2019) and Liu and Matsui (2022, both NPF and the contribution of organic aerosols in the remote atmosphere from the surface to the upper troposphere), and Weigel et al. (2021, NPF in the South Asian monsoon).

Thus, present knowledge on global surface UFP concentrations is mostly limited to local model studies and in situ measurements of particle size distributions (PSDs), from which UFP concentrations can be inferred. While the number of PSD measurements is increasing (Wu and Boor, 2021; Rose et al., 2021), they are still sparse and mostly not continuous over time. Furthermore, there are no clear methodological guidelines for measuring PSDs or particle number concentrations (PNCs) (Trechera et al., 2023), and measurement size limits vary greatly. However, new recommendations have recently been suggested (CEN/TS 17434:2020, 2020; CEN/TS 16976:2016, 2016; ACTRIS, 2021).

To generate a first, global, annually averaged UFP dataset for the years 2015–2017 we used the ECHAM/MESSy Atmospheric Chemistry model (EMAC; Jöckel et al., 2006), including gas-phase and heterogeneous chemistry with comprehensive chemical mechanisms, aerosol microphysics with size-resolved particulate matter and cloud interactions. Such data can be applied to investigate the impact of UFPs on public health, CCN formation and cloud properties, as well as for intercomparison studies with other regional and global models and datasets.

Several emission inventories describe the total emitted mass of aerosol and gas species on a global grid (e.g. Hoesly et al., 2018; Crippa et al., 2020; Granier et al., 2019). However, the inference of the number of emitted particles is very sensitive to their size distribution as small changes can lead to large deviations in the resulting particle number concen-

trations. Information on these size distributions is rare, and the uncertainties are high (Paasonen et al., 2016). For that reason we use existing information on PSDs of emitted particles from the literature and evaluate our results against measurement data in China, India, Europe, the United States and various remote regions.

Another challenge in the global modelling of UFPs is the limited model resolution. Studies showed that UFP concentrations return to background levels within a distance of about 1000 m from the source (e.g. Karner et al., 2010, for roadways). Thus, UFP concentrations can show sharp urban to rural gradients (e.g. Saha et al., 2021) that cannot be captured efficiently by a global model that is limited in the horizontal grid size. As a result, high local UFP concentrations in densely populated urban areas may be artificially diluted by the surrounding regions in the grid boxes. This may result in an underestimation of UFP concentrations in city centres, while concentrations in remote regions close to urban areas may be overestimated. This shortcoming in the evaluation of model results is studied in depth as the inability of localized measurements to represent the grid box environment (representation error) in Schutgens et al. (2016a, b, 2017).

The correlation between the underestimation of the model on the one hand and local high-resolution anthropogenic emissions at the measurement sites relative to the average anthropogenic emissions at model resolution on the other hand is used here to derive UFP concentrations at $0.1° \times 0.1°$ horizontal resolution. We show that this improves the agreement between observations and simulations, reduces the spatial representation error, and decreases inconsistencies introduced by the difficulties of the coarse model resolution to capture population density and air pollution gradients.

2 Global model and methods

The ECHAM/MESSy Atmospheric Chemistry (EMAC) model (Jöckel et al., 2006) is a combination of the fifth-generation European Centre Hamburg general circulation model, ECHAM5 (Roeckner et al., 2003), which serves as the dynamical base model, and the second version of the Modular Earth Submodel System, MESSy2 (Jöckel et al., 2010), comprising various submodels that describe the chemistry and physics of the atmosphere.

The simulation used for this study is performed at a spectral, horizontal resolution of T63 ($1.875° \times 1.875°$ or approx. 180×180 km at the Equator) with 31 vertical, hybrid terrain-following and pressure levels up to 10 hPa altitude and the surface level extending up to approximately 45–70 m above the surface, depending on latitude and season. The model simulation is "nudged" (Jeuken et al., 1996; Jöckel et al., 2006) towards meteorological reanalysis data of the years 2014–2017 (ERA-Interim; Berrisford et al., 2011) from the European Centre for Medium-Range Weather Forecasts (ECMWF).

Global anthropogenic emissions of reactive gases and aerosols at the surface from the simulated years are taken from the Community Emissions Data System (CEDS; McDuffie et al., 2020a, b). We consider primary emitted black carbon (BC), organic carbon (OC) and sulfate (SO_4; 2.5 % of SO_2 emissions according to Dentener et al., 2006) as direct aerosol sources at the surface. The CEDS anthropogenic emissions from the sectors energy generation (ENE), industries (IND), land transportation (TRA), domestic energy use (DOM), waste (WST), agricultural soils (AGR), solvent production and application (SLV; no primary particle emissions), and ship and other navigation (SHIP) are considered. Emissions from biomass burning (BB) and agricultural waste and residue burning (AWB) were calculated daily using the BIOBURN submodel based on observed dry matter burned and fire type compiled by Andreae (2019). The biomass burning emissions for OC and BC were increased by a factor of 4.48 and 2.8, respectively, based on the work of Pan et al. (2020) and a comparison with observations in the Amazon Basin (Holanda Bruna, personal communication, 2023). Aircraft emissions of reactive gases, BC and OC were taken from the CAMS global aviation emissions (CAMS-GLOB-AIR; Granier et al., 2019). Sea salt (see algorithm from Guelle et al., 2001) and dust emissions (see algorithm from Klingmüller et al., 2018) are calculated online using the submodel ONEMIS (Kerkweg et al., 2006). All emissions are distributed to six different emission height levels based on the description by Pozzer et al. (2009).

Aerosols are treated using the MESSy submodel GMXe (Pringle et al., 2010). Aerosol microphysics are based on aerosol size distributions with currently seven interactive lognormal modes that cover the typical size spectrum of aerosol species and differentiate into four hydrophilic (nucleation, Aitken, accumulation and coarse) and three hydrophobic (Aitken, accumulation and coarse) aerosol modes. All aerosols are approximated as spherical particles. The properties of aerosols in each mode are completely defined by the total mass (internal mixture of contributing species), density, number concentration, median radius and width of the lognormal distribution. After each simulation step aerosols may transfer between modes depending on size changes. Organic aerosol species are additionally described by the Organic Aerosol Composition and Evolution (ORACLE; Tsimpidi et al., 2018) submodel, taking into account the partitioning between aerosols and the gas phase. ORACLE distinguishes between primary and secondary organic aerosols from different sources and volatilities (in up to five logarithmically spaced saturation concentration bins, ranging from 10^{-2} to 10^{6} µg m^{-3}, depending on the emission sector).

Heterogeneous and gas-phase chemistry are treated with the submodel MECCA (Sander et al., 2019) with the Mainz Isoprene Mechanism (MIM1; Pöschl et al., 2000; Jöckel et al., 2006) as the chemical mechanism, comprising more than 100 gas-phase species and more than 250 reactions. Dry deposition, sedimentation and wet deposition are simu-

lated with the submodels DDEP, SEDI (both Kerkweg et al., 2006) and SCAV (Tost et al., 2006), respectively. The submodel NAN (Ehrhart et al., 2018) is used to estimate binary and ternary nucleation following Dunne et al. (2016), pure organic nucleation (Kirkby et al., 2016), and nucleation from oxidized organic species and sulfuric acid (Riccobono et al., 2014). The parameterization of ion-induced nucleation is included in NAN, using ion pair production and steady-state ion concentrations from the submodel IONS (Ehrhart et al., 2018). IONS calculates the ion pair production from galactic cosmic rays and from radon decay. The latter is obtained from the diagnostic radon (DRADON) submodel (Jöckel et al., 2010).

Aerosols at the surface simulated with the EMAC model have been extensively evaluated in many publications, with a focus on either $PM_{2.5}$ mass or aerosol optical depth (Pozzer et al., 2012, 2015; Lelieveld et al., 2019; Pozzer et al., 2022). Chowdhury et al. (2022) conducted an evaluation for aerosol optical depth, $PM_{2.5}$, and black carbon and organic aerosols in $PM_{2.5}$ using a similar setup as used in this study.

The number of emitted aerosols (N_{aer}) is calculated as

$$N_{\mathrm{aer}} = \frac{6 \cdot M_{\mathrm{aer}}}{\pi \cdot \rho_{\mathrm{aer}} \cdot d_{\mathrm{med}}^3} \cdot \exp\left(-4.5 \ln^2 \sigma_{\ln}\right), \tag{1}$$

where the emitted aerosol mass M_{aer} is given by the respective emission dataset. ρ_{aer} is the density of the considered aerosol species, and $\sigma_{\ln}$ is the width of the lognormal mode in the model. The fraction is just the geometrical derivation of the number of spherical particles from total mass, given a diameter d_{med}, while the exponential function corrects for the lognormal volume distribution (compare Eqs. 8.34 and 8.51 from Seinfeld and Pandis, 2016). The median diameter of the emitted particles (d_{med}) depends on the considered sector and species. As $N_{\mathrm{aer}} \propto 1/d_{\mathrm{med}}^3$, the number of emitted particles is highly sensitive to the emission median diameter; i.e. a doubling of the diameter leads to a reduction in the number of emitted particles by a factor of 8.

In order to emit the aerosols with a realistic size distribution for each sector, a detailed investigation of the emission size distributions is performed based on the findings of Paasonen et al. (2016). Paasonen et al. (2016) used an emission model (Amann et al., 2011) in combination with emission factors and size distributions from the literature in order to obtain global emission particle size distributions for different sectors. As the median emission diameter d_{med} is a global quantity in the EMAC model, we derived the median of the present global size distributions from Paasonen et al. (2016) and used them as d_{med} for the corresponding sectors in our model. The distributions along with their median diameters are depicted in Fig. 1.

Additionally, the aerosol median emission diameter from biomass burning and AWB is estimated to be 130 nm based on the average of multiple studies on biomass burning emissions summarized in a review (Reid et al., 2005), confirmed by Janhäll et al. (2010, who measured 120 nm) and the respective size distribution from Paasonen et al. (2016) for AWB (median diameter of 126 nm). Ship aerosol emissions are assumed to be represented by a median diameter of 40 nm based on studies by Kasper et al. (2007, who found 20–40 nm for low-speed marine diesel engines), Diesch et al. (2013, small nucleation mode from 10–20 nm and Aitken mode around 35 nm) and Petzold et al. (2008, 52 nm in fresh plume and up to 100 nm in aged plume). Aerosols from aircraft emissions are emitted at a diameter of 40 nm as well, based on studies from Petzold and Schröder (1998) and Petzold et al. (2003), who distinguished a mode between 30 and 45 nm and an additional smaller accumulation mode around 180 nm. Dust particles are emitted only in the accumulation and coarse modes according to Klingmüller et al. (2018) and play a negligible role in UFP concentrations (d'Almeida, 1987). For the emissions of sea salt we use the diameters from the algorithm of Monahan (1986), also only emitting particles in the accumulation and coarse modes.

As only a few measurements of PSDs are available, which can be used to directly infer UFP concentrations, measurements of total PNCs are additionally used for the model evaluation as they are often dominated by UFPs, especially close to UFP sources (e.g. Baldauf et al., 2016; Kumar et al., 2014). Figure 2 shows a typical simulated PSD (blue line) as the sum of the four soluble and three insoluble modes. The solid red line shows the upper bound for UFPs at 100 nm. The dashed red line is the variable lower bound, used exclusively for comparison to observations, as measurement devices entail a cut-off particle diameter below which no particles are detected. The published global UFP dataset includes arbitrarily small particles and does not use a lower cut-off value.

The UFP concentration in the simulation N_{UFP} is calculated using the particle number concentration $N_{\mathrm{tot},i}$, the width σ_i and the median diameter $D_{\mathrm{m},i}$ of each mode i:

$$N_{\mathrm{UFP}} = \sum_{i=1}^{7} \frac{N_{\mathrm{tot},i}}{2} \cdot \left\{ \mathrm{erf}\left(\frac{\ln\left(D_{\mathrm{up}}/D_{\mathrm{m},i}\right)}{\sqrt{2}\ln(\sigma_i)} \right) - \mathrm{erf}\left(\frac{\ln\left(D_{\mathrm{low}}/D_{\mathrm{m},i}\right)}{\sqrt{2}\ln(\sigma_i)} \right) \right\}, \tag{2}$$

where D_{up} is the fixed upper bound of 100 nm, and D_{low} is the variable lower detection limit associated with the measurement device below which no particles can be detected. The cut on the detection limit is applied on the simulation for comparisons with observations. For the final global dataset we report the total number of UFPs, and thus D_{low} is set to 0 nm, and the second error function in Eq. (2) equates to -1.

The total PNC is the sum of the particle number concentrations $N_{\mathrm{tot},i}$ for each mode (i.e. $D_{\mathrm{up}} = +\infty$, and the terms in the curly brackets in Eq. (2) add up to $+2$ for $D_{\mathrm{low}} = 0$). However, PNC measurements also have a lower cut-off value, which has to be considered for model evaluation when comparing simulated and measured PNCs.

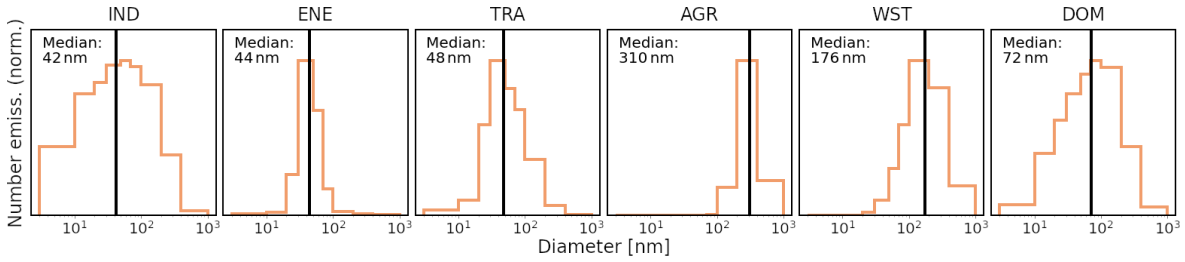

Figure 1. Normalized size distributions of primary emitted particles from different sectors (IND: industries, ENE: energy generation, TRA: land transportation, AGR: agricultural soils, WST: waste, DOM: domestic energy use) taken from Paasonen et al. (2016) with corresponding median diameters derived from these distributions (black line). The median diameters are taken as median diameters for the sector emissions in our simulation.

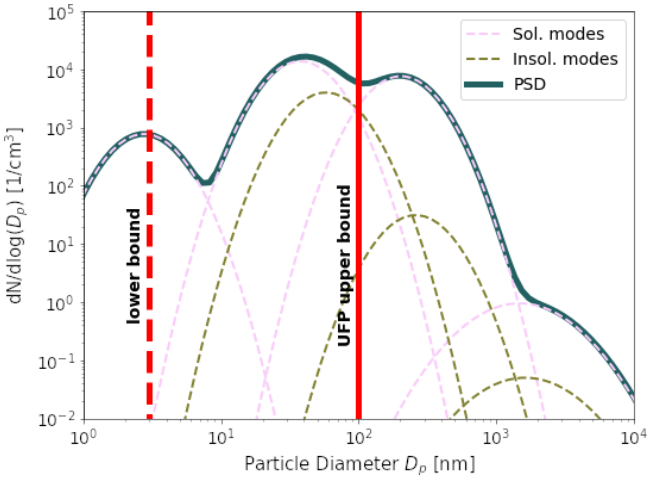

Figure 2. Typical particle size distribution (PSD) taken from the simulation in an urban region. The dashed lines represent the soluble and insoluble aerosol modes. The PSD is the sum of all these modes (blue line), typically dominated by the soluble modes. UFPs are defined as all particles with a diameter below 100 nm (right red line), while the total particle number concentration is the full integral over the PSD. For comparison between observed and simulated concentrations, the lower bound (dashed red line) is considered a cut-off, which depends on the detection limit of the measurement device. The final dataset includes all UFPs without lower bounds.

3 Observations

In order to evaluate the simulated UFP concentrations from the EMAC model, observations were collected from different stationary measurement sites at the Earth's surface with a focus on polluted regions. The simulation has been performed for the years 2015–2017 with 1 year of spin-up (2014), whereas we evaluated the simulation for the year 2015 only. Thus, if available, the simulations were compared to observations in 2015. However, to increase the number of available datasets to compare with simulation results, we additionally used annual averages of observed UFP concentrations and PNCs from all available years for the evaluation. This is noted accordingly in the following sections. Observational data were collected for UFP concentrations and PNCs and were compared to the respective calculated simulated values according to the lower cut-off value of the respective measurement devices. The sources of the observational data of UFPs (derived from PSDs) and PNCs are listed below.

3.1 EBAS

EBAS is a database for atmospheric measurement data operated by the Norwegian Institute for Air Research (NILU) and contains measurements for different programmes of which we used the following:

- The European Monitoring and Evaluation Programme (EMEP) monitors air pollutants in Europe.
- The Global Atmosphere Watch – World Data Centre for Aerosols (GAW-WDCA) is a data repository for microphysical, optical and chemical properties of atmospheric aerosol.
- The Aerosol, Clouds and Trace Gases Research Infrastructure (ACTRIS) contains long-term atmospheric measurement data.

The data were obtained from the EBAS database (http://ebas.nilu.no/, last access: 17 February 2022). We analysed all available PSDs (mostly in Europe and remote regions) and PNC measurements (Europe, North America and remote regions) taken in 2015.

3.2 Field measurements, literature and published datasets

We derived UFP concentrations from PSDs measured by groups involved in the present study in India, China and the Amazon rainforest. In India PSDs were measured in Delhi (Thamban et al., 2021), Mahabaleshwar and Hyderabad (both Sebastian et al., 2022). Measurements in China were taken in Shanghai (unpublished), Beijing (Liu et al., 2020), Lin'an (Shen et al., 2022) and Gucheng (Li et al., 2021). Additionally, we used measurements from the Amazon Tall Tower Observatory (ATTO) centrally located in

the rainforest in Brazil, about 150 km northeast of Manaus (Franco et al., 2022). The observational datasets are complemented by including literature and published datasets from China and India (Gani et al., 2020; Wu et al., 2008), as well as from the Atmospheric Tomography mission (ATom) aircraft campaign (Brock et al., 2019).

4 Results

Annual averages of modelled UFP (UFP_M) concentrations in 2015 on a global scale are displayed in Fig. 3, ranging from about 40 cm^{-3} over parts of the ocean to up to more than 12 000 cm^{-3} in China, India, Indonesia and Papua New Guinea (considering averages over model grid boxes). UFP_M concentrations are generally high across Europe, ranging from 2000 to 6000 cm^{-3}; however, they are lower than in several Asian hotspot areas. In North America, UFP_M concentrations are simulated to be higher along the East Coast, with additional hotspots in and around the big cities along the West Coast, reaching up to 8000 cm^{-3} in and around San Francisco and Los Angeles. We also simulate high UFP_M concentrations close to 10 000 cm^{-3} in the West Coast of South America and regional enhancements along the East Coast. Southern Australia, northern Africa and the Middle East (the Persian Gulf region) also show enhanced UFP_M concentrations exceeding 8000 cm^{-3}.

Continental polar regions in North America, Europe, Asia and Antarctica are simulated to have UFP_M concentrations mostly below 500 cm^{-3} due to the absence of pollution particle sources. Low UFP_M concentrations (down to 150 cm^{-3}) are also simulated across the Amazon rainforest and in major desert regions (e.g. the Sahara). However, there is a lack of measurement data of PNCs and UFP concentrations in desert regions that hinders the evaluation of the model results. Low UFP concentrations in the boundary layer over the Amazon forest have been reported previously and have been attributed to missing sources of primary UFPs and the growth of secondary particles during transport from the upper troposphere through the condensation of oxidized organic species, reaching the boundary layer through convective downdrafts (Zhao et al., 2020; Wang et al., 2016; Andreae et al., 2018).

UFP_M concentrations over the oceans are highly variable, with relatively high values exceeding 2500 cm^{-3} over the Pacific and Indian oceans downwind of pollution sources on land and very low values below 50 cm^{-3} over the Southern Ocean and tropical Atlantic and Pacific oceans. Low UFP concentrations in the tropical ocean environment have been observed by the ATom aircraft campaign as well, potentially caused by the efficient removal of small particles by coagulation and again the downward transport of aged secondary particles from the upper troposphere (Williamson et al., 2019).

PNCs were previously modelled by Gordon et al. (2017) at relatively low global resolution, Saha et al. (2021) for the United States only and Chen et al. (2021) with a focus on eastern Asia. Gordon et al. (2017) concentrated on cloud condensation nuclei and averaged over a vertical column of 460 m. We generally simulate higher concentrations compared to Gordon et al. (2017), mostly capturing UFP hotspots, in accordance with observations, especially after the redistribution based on anthropogenic emissions (see Sect. 4 and 4.2). The comparably lower concentrations simulated by Gordon et al. (2017) might partially result from the larger vertical column in the simulation, the coarser resolution or the different emission diameters (globally 60 nm for all fossil-fuel-related emissions). Our simulated UFP concentrations agree very well with the PNC simulation from Chen et al. (2021) in most continental regions, especially in Europe, North and South America, Africa, Australia, and eastern Asia (which they focused on). However, simulated PNCs in India are considerably lower than our UFP concentrations (supported by observations; see Sect. 4.1.3). Additionally, we simulate higher UFP concentrations at marine southern mid-latitudes (in reasonable agreement with measurements taken during the ATom campaign; see Sect. 4.1.5) than Chen et al. (2021).

The simulated spatial distribution of UFPs over the contiguous United States matches that of Saha et al. (2021). They used a land use regression model to produce a high-resolution (200 × 200 m) product of UFP concentrations. We reach similar values in the urban regions in the United States after the redistribution based on anthropogenic emissions as described in Sect. 4.2; however the values are still lower than the highest values simulated by Saha et al. (2021). The difference might be due to the fact that UFP concentrations are a subset of PNCs. Ketzel et al. (2021) simulated PNCs at the street- and address-level on the same order of magnitude as our simulation up to the urban background level but with much higher peak values, reaching more than 30 000 cm^{-3} in traffic hotspots, which we cannot resolve. Our simulated UFP concentrations are much lower than the modelled results from Fountoukis et al. (2012), which reach around 20 000 cm^{-3}, even for background regions in Europe in May 2008, and up to more than 100 000 cm^{-3} in local hotspots in southeastern Europe. However, the general increasing trends from western to eastern Europe agree.

Trechera et al. (2023) analysed observations of PNCs and UFP concentrations in Europe from 2017 to 2019, focusing on daily and seasonal patterns, UFP drivers, and regional trends. They again find increasing UFP concentrations from northern to southern and from western to eastern Europe. Our simulation also exhibits the west–east tendency in Europe, however no clear pattern from north to south. Seasonality and drivers of UFP concentrations and composition will be the subject of follow-up studies.

UFPs have widely differing size distributions across the globe. Figure 4 illustrates this based on three size bins, i.e. 1.7–20, 20–50 and 50–100 nm. Freshly nucleated particles between 1.7 and 20 nm mostly dominate in remote environ-

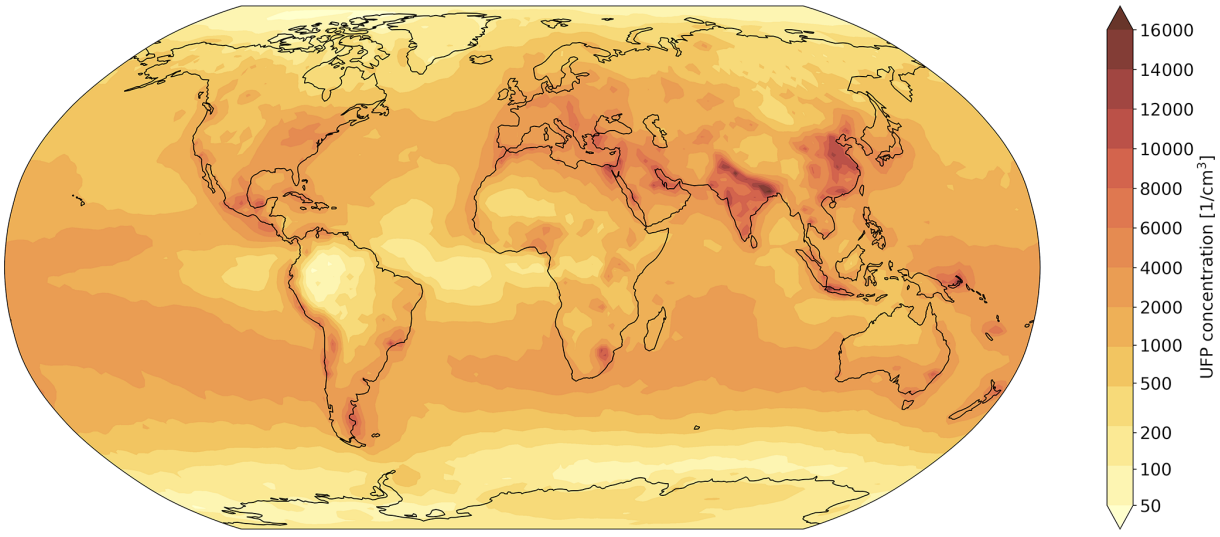

Figure 3. Annual average of global UFP concentrations simulated with EMAC for the year 2015 at model resolution of 1.875° × 1.875° and from the lowest vertical model level (surface level).

ments, especially over oceans. PSDs usually peak at diameters between 20 and 50 nm in polluted regions, representing a mixture of freshly emitted primary particles from fossil fuel combustion and rapidly grown secondary particles. Biomass burning particles are typically emitted at larger diameters (see Fig. 1). Additionally, high concentrations of organic vapours lead to strong condensational growth in forest regions. Thus, UFPs are dominated by 50–100 nm particles there.

The interannual variability in UFP concentrations is presented in Fig. 5. We observe strong interannual variation, exceeding 1000 cm^{-3} and (up to 50 %) along the Intertropical Convergence Zone (ITCZ), which is mostly caused by meteorological differences in the different years, potentially caused by the strong El Niño in 2015, followed by weaker La Niña and El Niño events in 2016 and 2017. The meteorological influence on UFP concentrations could be the basis for future studies. We additionally find absolute interannual variation exceeding 1000 cm^{-3} over polluted regions, although below 20 % in relative terms. This is mostly due to a decreasing trend in emissions over southern and eastern Asia, Europe, and the United States. However, we observe an increasing trend in UFP concentrations over parts of Africa, especially over Nigeria and South Africa.

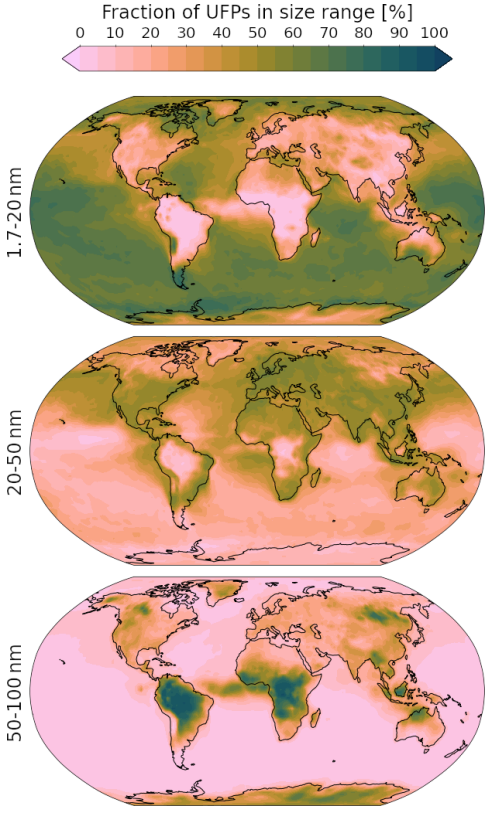

Figure 4. Fraction of UFPs in different size ranges, representing freshly nucleated particles (1.7–20 nm), fossil fuel emissions or grown nucleation particles (20–50 nm), and further grown or larger emitted particles (50–100 nm).

4.1 Evaluation

In the following, we present the evaluation of the simulated UFP_M concentrations based on observational data. Section 4.1.1 to 4.1.4 evaluate urban and rural regions in four comparably highly polluted regions for which measurement data are available, namely Europe, North America, India and China. In Sect. 4.1.5 remote regions in polar, forest, mountain and ocean environments with a lower population density are evaluated. Mountain environments are defined covering altitudes from 1500 to 3000 m a.s.l., while measurements

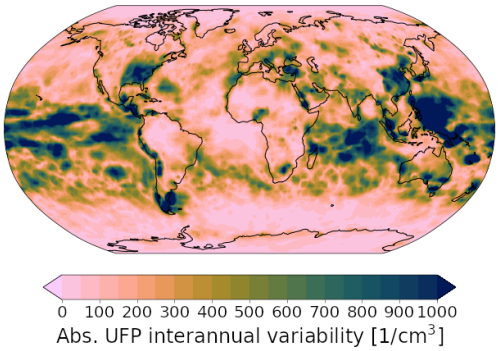

Figure 5. Absolute interannual variation in UFP concentrations calculated based on the years 2015–2017. It is defined by the maximum minus the minimum annually averaged UFP concentrations.

above 3000 m a.s.l. were excluded as they are mostly located in the free troposphere, and this study concentrates on boundary layer processes and the respective evaluation.

Annual averages of observed UFP (UFP_O) concentrations and PNCs (PNC_O) were either derived from daily PSDs (by integrating the number of aerosol particles per size bin from the lowest measurement bin up to the bin crossing the upper size threshold of 100 nm) and PNCs – removing outliers differing by a factor greater than 10 from the median value and subsequently calculating the annual average – or directly provided. The daily averaged number concentrations of the model aerosol modes were integrated for the same size region as the observations (from the lower detection limit of the measurement device up to the highest measurement bin with a mean diameter below 100 nm) according to Eq. (2). UFP_M concentrations were sampled at the vertical grid box covering the measurement site altitude.

The evaluation in this section concentrates on the modelled (UFP_M or PNC_M) and observed (UFP_O or PNC_O) concentrations. The downscaled (i.e redistributed within each grid box) concentrations (UFP_R or PNC_R) are the subject of Sect. 4.2. We used three different statistical measures for the evaluation based on daily model output and observations if available:

- PF2, percentage of modelled values that are simulated within the range of a factor of 2 of the observed values;
- NRMSE, root mean squared error (RMSE) normalized by the range of the observations; and
- $\overline{M/O}$, geometric mean of the ratio between the modelled (M) and observed daily mean (O).

4.1.1 Europe

UFP_O concentrations in Europe were derived from daily PSDs provided by the EBAS database. An overview of the different measurements in Europe and a comparison to UFP_M are presented in Table 1. We used all available observations from the EBAS database from 2015 in Europe from rural and urban stations. The remote stations as defined above are excluded here and are discussed separately in Sect. 4.1.5. Additionally, we excluded measurements in Athens (GR) and Preila (LT) due to apparent inconsistencies in the observational datasets.

The simulation shows reasonable agreement with the observations at most measurement stations with $PF2 \geq 40\,\%$, $NRMSE \leq 0.4$ and $0.5 \leq \overline{M/O} \leq 2.0$. However, there are some exceptions. At the measurement stations of Madrid, Leipzig-Eisenbahnstrasse, Leipzig-Mitte and Dresden-Nord, the model strongly underestimates the UFP concentrations. This is due to a combination of two effects. Firstly, UFP concentrations are typically related to anthropogenic emissions (see Sect. 4.2 for details). The high UFP concentrations in the densely populated urban centres are artificially diluted in the simulation by lower concentrations in the surroundings covered by the grid box. This spatial representation error after Schutgens et al. (2016a) can partly be corrected for by redistributing UFP concentrations using high-resolution anthropogenic emission datasets, discussed in detail in Sect. 4.2. Secondly, the measurements were performed close to busy streets (the Leipzig-Eisenbahnstrasse, Leipzig-Mitte and Dresden-Nord sites particularly measure traffic emissions) with high primary UFP emissions from vehicles, which would require impracticable street-level horizontal resolution to resolve.

The model overestimates UFP_M concentrations at the stations of L'Observatoire pérenne de l'environnement (OPE; France) and Finokalia (GR). OPE is located at a remote region close to Nancy, and the grid box is thereby highly influenced by the urban region. Finokalia on the other hand is located in a rural environment close to the coast of the island Crete. The interference of the oceanic influence and surrounding enhanced anthropogenic emissions from the island leads to enhanced UFP concentrations within the grid box.

Multiple measurements in one city provide an interesting case of the variability in UFPs within one modelled grid box. Measurements were performed at four different locations in Leipzig (shown in Fig. 6), varying by up to a factor of 3, while simulated UFP_M concentrations (dashed grey line) approximately coincide with the observations taken at some distance from heavy traffic locations (Leipzig). The station at Leipzig-Eisenbahnstrasse is at a curbside and measures very high UFP_O concentrations. It can be noted that the model is capable of reproducing urban background conditions, i.e. the average over urban regions and their surroundings in the grid box, while not replicating local UFP hotspots, for example roadsides or near industrial emitters, due to limited horizontal resolution. It is expected that dilution and coagulation during atmospheric transport from these hotspots to the surroundings will quickly reduce the UFP concentrations to levels that are realistically represented by the urban back-

Table 1. Summary of observations of UFP (UFP_O) concentrations (cm^{-3}) derived from PSDs across Europe for 2015, with data archived in the EBAS database. The geographical location is indicated by latitude (Lat) and longitude (Long), and the elevation of the site above the sea surface is indicated by the altitude a.s.l. in metres (Alt). The lower cut-off value (Cut) from the measurement device (also applied on the simulation) is expressed in nanometres. The annual averages of the UFP_O and UFP_M concentrations for the grid box encompassing the station are compared, and different measures of agreement are listed. The same comparisons are performed after the redistribution of the model (Redistributed model, UFP_R), which are discussed in detail in Sect. 4.2. All included measurement stations contained at least 200 d of valid measurements in 2015. Abbreviations: DD – Dresden, NOAK – National Atmospheric Observatory Košetice, ECO – Environmental-Climate Observatory, LE – Leipzig, OPE – Observatoire pérenne de l'environnement.

	Observations					Model results				Redistributed model			
Station	Lat	Long	Alt	Cut	UFP_O	UFP_M	PF2	NRMSE	$\overline{M/O}$	UFP_R	PF2	NRMSE	$\overline{M/O}$
Annaberg-Buchholz (DE)	50.57	13.0	545	9.4	6649	3597	55	0.21	0.55	3317	49	0.22	0.51
Cabauw Zijdeweg (NL)	51.97	4.93	1	9.1	6324	4539	77	0.22	0.72	3828	62	0.26	0.6
DD-Nord (DE)	51.06	13.74	120	4.8	10 526	4289	29	0.34	0.39	7690	67	0.25	0.7
DD-Winckelmannstr (DE)	51.04	13.73	112	9.4	5474	4218	85	0.16	0.78	7562	77	0.22	1.39
ECO Lecce (IT)	40.34	18.12	36	9.4	5372	3741	59	0.36	0.62	4821	62	0.37	0.8
Finokalia (GR)	35.34	25.67	250	8.6	1421	3628	34	0.6	2.3	3917	28	0.67	2.48
Hohenpeissenberg (DE)	47.8	11.01	985	9.4	2302	2479	78	0.25	1.08	2234	76	0.23	0.97
K-puszta (HU)	46.58	19.35	125	6.0	4040	5127	67	0.27	1.32	4966	66	0.26	1.28
LE-Eisenbahnstr (DE)	51.35	12.41	120	4.8	14 410	4358	15	0.37	0.3	5020	23	0.35	0.34
LE-Mitte (DE)	51.34	12.38	111	4.8	10 624	4251	27	0.34	0.39	5521	47	0.3	0.5
LE-West (DE)	51.32	12.3	122	4.8	6222	4451	74	0.21	0.69	4686	77	0.21	0.73
Leipzig (DE)	51.35	12.43	118	4.8	4882	4300	88	0.17	0.86	4953	91	0.17	0.99
Madrid (ES)	40.46	−3.73	669	14.4	11 311	2916	22	0.17	0.28	6192	59	0.15	0.59
Melpitz (DE)	51.53	12.93	87	4.8	7018	4343	72	0.19	0.62	4400	72	0.19	0.63
Montseny (ES)	41.78	2.36	700	8.9	3056	2375	69	0.21	0.78	2371	69	0.21	0.78
NOAK Kosetice (CZ)	49.58	15.08	534	8.6	2569	4332	57	0.3	1.79	3701	66	0.24	1.53
Neuglobsow (DE)	53.14	13.03	62	9.4	2808	3515	69	0.17	1.3	2986	74	0.15	1.11
OPE (FR)	48.56	5.5	392	9.7	1834	2865	63	0.32	1.6	2786	64	0.31	1.55
Prague-Suchdol (CZ)	50.12	14.38	277	5.6	6421	4412	74	0.15	0.7	6124	89	0.13	0.97
SIRTA Palaiseau (FR)	48.71	2.16	162	10.0	4239	3441	82	0.2	0.84	5391	79	0.24	1.31
Schauinsland (DE)	47.9	7.92	1205	9.4	1545	1833	78	0.19	1.22	1783	80	0.19	1.19
Vielsalm (BE)	50.3	6.0	496	8.8	2082	2596	75	0.22	1.26	2628	73	0.23	1.27

ground (e.g. Karner et al., 2010, finding a distance of 1000 m for roadways). This is in agreement with a study from Salma et al. (2014), showing measured UFP concentrations at different locations across Budapest, Hungary. They measured on average a factor of 3 higher UFP concentrations in the city centre compared to the urban background and an additional factor of 2 higher concentrations in street canyons.

4.1.2 North America

In North America only measurements of PNCs are available. Annual averages of observed PNCs (PNC_O) at urban sites in the United States are taken from a study by Saha et al. (2021). The measurements were performed in different years, from 2009 to 2016. The results are summarized in Table 2. We note that the model again underestimates PNC_O at central urban stations, mostly by a factor ranging from 1.5 to 2.5.

Additional observations of PNC_O in the United States and Canada were obtained from the EBAS database providing daily measurements. They are compared to annual averages of the simulation for days with valid measurements, shown in Table 3. PNC_M in Bondville, Egbert and at the Appalachian State University (ASU) agree reasonably well with the ob-

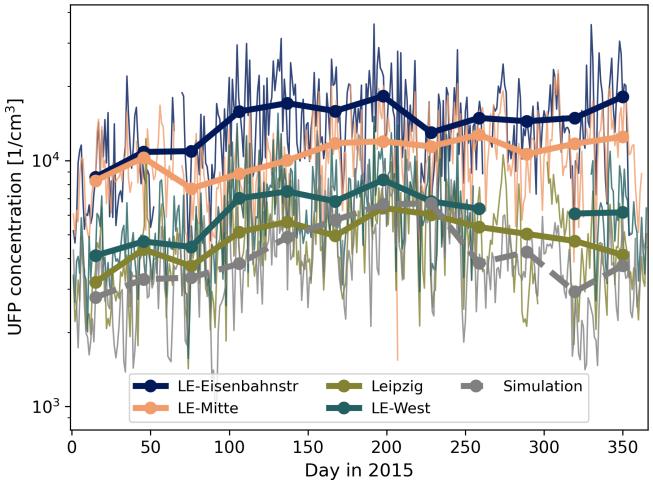

Figure 6. Monthly averaged UFP concentrations in the simulation (grey, dashed) and measured at different stations in Leipzig, Germany (thick, solid lines). The daily fluctuating UFP concentrations are shown with thin, transparent lines in the same colour.

Table 2. Summary of observations of PNCs (annual averages, cm^{-3}) in urban regions across the United States for different years taken from a study by Saha et al. (2021). The geographical location is indicated by latitude (Lat) and longitude (Long). The annual averages of observed (PNC_O) and modelled (PNC_M) PNCs (2015 for PNC_M, variable years for the observations) for the grid box encompassing the station are compared. The measurements applied a cut-off minimum diameter (Cut, in nanometres). The same cut-off was used to calculate simulated PNC_M. Simulated PNCs after the emission-sector-based redistribution are displayed as well (PNC_R), discussed in Sect. 4.2.

Location	Lat	Long	Year	Cut	PNC_O	PNC_M	PNC_R
Rochester (NY)	43.14	−77.54	2013	10	4450	3799	6294
Boston (MA)	42.33	−71.10	2016	10	12 200	4614	9169
Somerville (MA)	42.40	−71.09	2009	6	10 000	4687	8640
Queens (NY)	40.73	−73.82	2009	20	8210	4787	12 722
Long Island (NY)	40.74	−73.58	2009	20	7600	4787	9975
Livermore (CA)	37.69	−121.78	2012	7	8220	6090	6553
Red Wood (CA)	37.48	−122.20	2015	7	11 910	6090	9757
San Pablo (CA)	37.96	−122.36	2012	7	10 480	6090	12119
Santa Rosa (CA)	38.44	−122.71	2012	7	8660	6090	11 526
Anaheim (CA)	33.83	−117.94	2016	7	13 950	8019	12 100
Central LA (CA)	34.07	−118.23	2016	7	17 780	8019	14 929
Compton (CA)	33.90	−118.21	2012	7	14 000	8019	14 916
Rubidoux (CA)	34.00	−117.42	2016	10	12 930	7975	11 858

Table 3. Summary of observations of PNC_O (cm^{-3}) across the United States and Canada in 2015, with data archived in the EBAS database. The geographical location is indicated by latitude (Lat) and longitude (Long), and the elevation of the site above the sea surface is indicated by the altitude a.s.l. in metres (Alt). The annual averages of PNC_O and PNC_M for the grid box encompassing the station are compared, and different measures of agreement are listed. The same comparisons are performed after the redistribution of the model (Redistributed model), which are discussed in Sect. 4.2. All included measurement stations contained at least 250 d of valid measurements in 2015. There is no particle size cut-off value given in the datasets, and thus none is applied on the simulation. Abbreviations: ASU – Appalachian State University, SGP – Southern Great Plains observatory.

	Observations				Model results				Redistributed model			
Station	Lat	Long	Alt	PNC_O	PNC_M	PF2	NRMSE	$\overline{M/O}$	PNC_R	PF2	NRMSE	$\overline{M/O}$
ASU, Boone (NC, US)	36.21	−81.69	1076	2930	2471	58	0.26	0.81	3317	55	0.3	1.09
Bondville (IL, US)	40.05	−88.37	213	4095	4130	55	0.26	0.96	4343	55	0.27	1.01
Egbert (ON, CA)	44.23	−79.78	255	4962	3238	53	0.26	0.68	2775	49	0.27	0.58
SGP E13 (OK, US)	36.60	−97.48	318	3600	6966	40	0.61	1.82	7457	38	0.67	1.95
Trinidad Head (CA, US)	41.05	−124.15	107	1526	2882	48	0.59	1.8	2800	49	0.57	1.75

servations with respect to the aforementioned criteria (see Sect. 4.1.1), while at the Southern Great Plains (SGP) observatory and at Trinidad Head the concentrations are overestimated by the model. The SGP site is located in the middle of wheat fields and pastures and is thereby efficiently shielded from major UFP sources in the encompassing grid box. The Trinidad Head measurement was performed directly at the Californian coast, and the corresponding grid box is influenced by a mixture of anthropogenic, rural and oceanic influences, leading to strong UFP gradients (comparable to Finokalia in Europe).

4.1.3 India

Annually averaged UFP_O concentrations in Delhi (Thamban et al., 2021), Mahabaleshwar and Hyderabad (both from Sebastian et al., 2022) were obtained from a collaboration with groups performing field measurements. Additionally, we adopted daily measurements of PSDs from Gani et al. (2020) for the Indian Institute of Technology Delhi (IITD), which we converted to UFP concentrations and combined with the measurements of Thamban et al. (2021). The evaluation for India is summarized in Table 4.

The simulation grid cell covering Delhi underestimates UFP_O concentrations at all three urban measurement stations in Delhi. The higher UFP_O concentrations over the IITD compared to the two other measurements may be due to its proximity to a major highway. In contrast, our simulations are biased high over Hyderabad. The measurement station in Hyderabad is a suburban university campus, approximately 15 km from the city centre, where UFP concentrations are expected to be significantly reduced compared to the downtown regions with strong traffic emissions. The consequent UFP gradients may not be adequately resolved by our model cal-

Table 4. Summary of UFP_O concentrations (cm^{-3}) derived from PSDs in India for different years. The geographical location is indicated by latitude (Lat) and longitude (Long). The annual averages of UFP_O and UFP_M concentrations (2015 for UFP_M, variable years for the observations) for the grid box encompassing the station are compared. The measurements applied a cut-off minimum diameter (Cut, in nanometres). The same cut-off was used to calculate simulated UFP_M. Simulated UFP concentrations after the emission-sector-based redistribution are displayed as well (UFP_R), which are discussed in Sect. 4.2. Abbreviations: IITM – Institute of Information Technology & Management, IITD – Indian Institute of Technology Delhi, MRIU – Manav Rachna International University.

Station	Lat	Long	Year	Cut	UFP_O	UFP_M	UFP_R	Reference
Delhi IITM	28.61	77.1	2018/2019	14.1	19 750	15 339	28 789	Thamban et al. (2021)
Delhi IITD	28.55	77.19	2017/2018/2019	14.1	42 972	15 339	24 917	Thamban et al. (2021), Gani et al. (2020)
Delhi MRIU	28.45	77.28	2018/2019	14.1	17 350	15 339	15 959	Thamban et al. (2021)
Mahabaleshwar	17.92	73.66	2015	5.5	2441	2248	2316	Sebastian et al. (2022)
Hyderabad	17.46	78.32	2019/2020/2021	10	4680	6350	11 131	Sebastian et al. (2022)

culations (spatial representation error after Schutgens et al., 2016a).

4.1.4 China

Observations of PSDs in China were obtained through collaboration with relevant groups for Shanghai (unpublished), Beijing in 2018/19 (Liu et al., 2020), Lin'an (Shen et al., 2022) and Gucheng (Li et al., 2021). Additionally, we included observations from Beijing from 2004–2006 (Wu et al., 2008). We compare the UFP concentrations derived from our simulation to the PSD measurements from these sites. The results are summarized in Table 5.

UFP_M concentrations in Shanghai and Beijing are slightly lower (approximately 20 %) than UFP_O concentrations for the years closest to 2015 (2014 for Shanghai, 2018/19 for Beijing), unlike other urban locations discussed above. However, UFP_O concentrations in Beijing from 2004–2006 are underestimated by more than a factor of 2 by UFP_M. A probable reason for this is the various air pollution reduction measures in place in China, especially in Beijing. In Beijing, $PM_{2.5}$ concentrations decreased from 89 $\mu g\,cm^{-3}$ in 2013 to 58 $\mu g\,cm^{-3}$ in 2017 and 42 $\mu g\,cm^{-3}$ in 2019 (Zeng et al., 2019; Lu et al., 2020), implying a simultaneous reduction in UFP sources. Due to the air pollution reduction measures, industrial areas are also moved further away from city centres, potentially decreasing the association with UFP concentrations (see also Sect. 4.2).

UFP_M overestimates UFP_O strongly in Lin'an and slightly in Beijing's suburban Gucheng. Lin'an is influenced by the neighbouring city of Hangzhou with approximately 10 million inhabitants, Gucheng by sharing the grid box with central Beijing.

4.1.5 Remote regions

We considered remote measurements over the open ocean, in forests, on mountains and at polar sites, of both PNCs and UFP concentrations. The simulation and measurement results are summarized in Table 6. Simulated average concentrations are all within a factor of 2 of the observations. In particular, the northern hemispheric polar regions show good agreement, while there is a stronger overestimation and underestimation of UFP_O at the two measurement stations in Antarctica, both at elevated altitudes.

The annual average forest UFP_O concentrations at ATTO in Brazil (Franco et al., 2022) and Hyytiälä (EBAS database) are both underestimated by the simulation. The timeline analysis of the measurements in the Amazon forest (ATTO) shows this pronounced underestimation only in winter; i.e. UFP_M shows a stronger seasonality than UFP_O. The potential causes will be the subject of future studies, also considering data from an upcoming measurement campaign.

Measurements over the open ocean were taken from the ATom aircraft campaign (Brock et al., 2019), conducted in different seasons from 2016 to 2018. We collected all measurements that were performed below 200 m over the ocean and compared them to daily averaged UFP_M concentrations in the lowest vertical model level of the corresponding horizontal grid cell at the respective day of the year. UFP_O concentrations over the Southern Ocean are mostly underestimated by the simulation, while concentrations over the Pacific are overestimated. Considering generally higher UFP_M concentrations over the Pacific Ocean and lower UFP_M concentrations over the Southern Ocean (compare Fig. 3), the open-ocean UFP variance seems to be overestimated by the model.

4.1.6 Global

Figure 7 summarizes the evaluation results of all measurement stations presented and compares the annual averages of the observed to the simulated UFP concentrations in a scatterplot. The shapes of the symbols represent the five studied regions. Population density data (represented by the colour scheme in Fig. 7) are taken from CIESIN (2018), sampled at the measurement stations with a resolution of $0.1° \times 0.1°$.

The logarithms of UFP_O and UFP_M concentrations are correlated by $r = 0.93$ ($r = 0.76$ excluding remote regions), while the RMSLE (root mean square logarithmic error) is

Table 5. Summary of UFP_O concentrations (cm^{-3}) derived from PSDs in China for different years. The geographical location is indicated by latitude (Lat) and longitude (Long). The annual averages of UFP_O and UFP_M concentrations (2015 for the simulation, variable years for the observations) for the grid box encompassing the station are compared. The measurements applied a cut-off minimum diameter (Cut, in nanometres). The same cut-off was used to calculate simulated UFP_M. Simulated UFP concentrations after the emission-sector-based redistribution are displayed as well (UFP_R), which are discussed in Sect. 4.2.

Station	Lat	Long	Year	Cut	UFP_O	UFP_M	UFP_R	Reference
Shanghai	31.17	121.43	2014	13.4	12 800	10 850	23 623	Unpublished
Beijing	39.94	116.29	2018/2019	5.6	14 812	11 489	20 123	Liu et al. (2020)
Beijing	39.9	116.38	2004–2006	3.0	24 900	11 408	21 041	Wu et al. (2008)
Lin'an	30.28	119.75	2015	3.8	4928	11 815	12 447	Shen et al. (2022)
Gucheng	39.15	115.73	2018/2019	12.9	8284	10 678	9680	Li et al. (2021)

Table 6. Summary of UFP_O concentrations (cm^{-3}) and PNC_O in remote regions. Four different settings are distinguished, namely ocean, forest, mountain and polar. The geographical location is indicated by latitude (Lat) and longitude (Long), and the elevation of the site above the sea surface is indicated by the altitude a.s.l. in metres (Alt). The annual averages of the observed (Obs) and simulated (Mod) concentrations for the grid box encompassing the station are compared, and different measures of agreement are listed (see Table 6). We applied the measurement detection limit on the simulation for all UFP concentrations, while information on the detection limit was not available for the PNC measurements.

Station	Setting	Lat	Long	Alt	Meas	Obs	Mod	PF2	NRMSE	$\overline{M/O}$	Reference
ATom campaign	Ocean	–	–	< 200	UFP	403	800	–	–	–	Brock et al. (2019)
ATTO (Brazil)	Forest	−2.14	−59.0	120	UFP	376	199	–	–	–	Franco et al. (2022)
BEO Moussala (BG)	Mountain	42.18	23.59	2925	UFP	542	940	45	0.51	1.58	EBAS
Hyytiälä (FI)	Forest	61.85	24.3	179	UFP	1430	1140	59	0.21	0.77	EBAS
Sammaltunturi Pallas (FI)	Polar	67.97	24.12	565	UFP	556	489	43	0.24	0.71	EBAS
Trollhaugen (NO)	Polar	−72.02	2.53	1309	UFP	154	62	31	0.23	0.36	EBAS
Värriö (FI)	Polar	67.75	29.61	390	UFP	697	800	44	0.34	0.93	EBAS
Zeppelin mountain (NO)	Polar	79.9	11.86	473	UFP	161	185	40	0.42	0.55	EBAS
Zugspitze (DE)	Mountain	47.41	10.98	2650	UFP	944	655	57	0.22	0.65	EBAS
Alert (NU, CA)	Polar	82.50	−62.34	2182	PNC	205	279	47	0.26	1.48	EBAS
Barrow (AK, US)	Polar	71.32	−156.61	11	PNC	277	417	33	0.44	0.98	EBAS
South Pole	Polar	−90.00	−24.80	2841	PNC	192	238	56	0.21	1.5	EBAS

0.55.[1] The geometric mean of the ratio between the modelled and observed mean values is $\overline{M/O} = 0.82$.

In remote areas all simulated concentrations are within a factor of 2 of the observed ones. For these areas the population density (and respective anthropogenic emissions) within the encompassing grid box is mostly uniform at low numbers of inhabitants; i.e. the grid cells only cover remote areas. Thus, the grid cell average of UFP concentrations is not influenced by densely populated and typically much more polluted regions.

All other measurement stations considered have in common that the encompassing grid boxes include an urban city centre with its surroundings and thus have high variance in anthropogenic emissions within the grid box. Figure 7 indicates a link between local population density and UFP concentrations. In fact, the logarithm of the population density is positively correlated to the logarithm of the UFP_O concentrations in non-remote regions with $r = 0.80$. Thus, it can be expected that the actual UFP concentrations in grid boxes encompassing urban regions and its surroundings are non-uniform, with higher UFP concentrations at higher population density and lower UFP concentrations at lower population density. This inability of in situ observations to represent the grid box environment is defined as the spatial representation error and is studied by Schutgens et al. (2016a) and was found to be the strongest close to sources, in agreement with our evaluation results.

The spatial representation error is illustrated in Fig. 7. At low UFP_O concentrations in non-remote regions the local population density is lower (background, suburban and rural stations in grid boxes including urban centres), while UFP_M concentrations are higher than UFP_O concentrations ($\overline{M/O} = 1.32$ for a population density smaller than 100 individuals km^{-2}), as the model grid boxes are influenced by the urban regions. At higher UFP_O concentrations population density increases as well, and the simulation underestimates UFP_O concentrations on average by a factor of almost 2 ($\overline{M/O} = 0.62$ for a population density in excess

[1] We use the correlation and RMSE of the logarithmic values here as several orders of magnitudes are covered, and the influence of the lower UFP concentrations would be negligible otherwise.

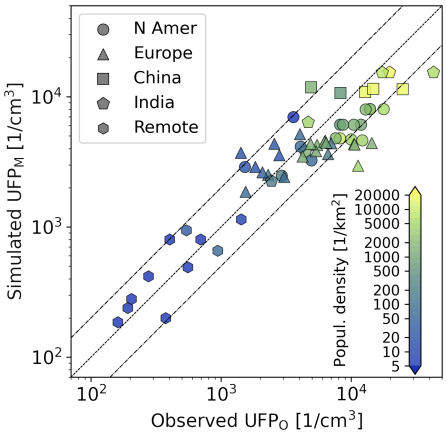

Figure 7. Summary of all measurement stations in a scatterplot showing observed UFP_O concentrations on the x axis and simulated UFP_M concentrations on the y axis. Different symbols indicate the different regions. The colour represents the local population density, sampled at the measurement stations with a resolution of $0.1° \times 0.1°$.

of 1000 individuals km^{-2}), as these urban stations are surrounded by suburban and rural regions that lower the simulation grid cell average of UFP_M concentrations.

The main cause of the spatial representation error is the limited model resolution of approx. 180×180 km (at the Equator). Consequently, the correlation between the logarithm of the local population density and UFP_M concentrations in non-remote regions is only $r = 0.57$, thus much lower than the correlation to UFP_O concentrations. To overcome this, an increase in model resolution of at least a factor of 3 (in one dimension) would be necessary, which would lead to an unreasonably high demand of computing time. Thus, an alternative approach was developed to mimic a resolution increase, by retroactively (after the simulation) redistributing UFP_M concentrations per grid box based on local high-resolution primary anthropogenic emissions relative to the grid box averaged primary anthropogenic emissions, guided by observations. This is discussed in the following section.

4.2 Downscaling based on primary anthropogenic emissions

Our results, in line with the observations, corroborate that UFP concentrations at the Earth's surface are strongly influenced by anthropogenic activity. Although our access to long-term measurements is limited, the data available from several urban stations show a high variance in UFP_O concentrations among different sites in a city (e.g. for Leipzig, Germany, and Los Angeles, the United States), being enhanced when model grid boxes contain urban and rural environments (e.g. Salma et al., 2014). Population density and UFP_O concentrations are highly correlated, while the evaluation of UFP_M concentrations indicates discrepancies due to sharp gradients of anthropogenic emissions within areas covered by the model grids.

Primary anthropogenic emissions (PAEs) from the CEDS database are available at a resolution (that is higher than the model resolution) of $0.5° \times 0.5°$ (hereafter referred to as $PAE_{CEDS;0.5}$) and were regridded to the simulation mesh (resulting in grid box averaged emissions $PAE_{CEDS;GB}$). Primary anthropogenic emissions from the Emissions Database for Global Atmospheric Research (EDGAR) v6.1 (Crippa et al., 2022) are available at an even higher resolution of $0.1° \times 0.1°$ (hereafter referred to as $PAE_{EDGAR;0.1}$). Studies showed that locally enhanced UFP concentrations usually reach (urban) background levels within 1000 m from sources (e.g. Karner et al., 2010), and the curbside UFP concentrations are highly localized. Hence, this section aims to use local $PAE_{CEDS;0.5}$ and $PAE_{EDGAR;0.1}$ and the relation to the respective grid box average at coarser resolution to fine-tune the simulation results guided by the observations, gaining improved resolution (downscaling) and closer agreement with observations (reducing the spatial representation error), especially in urban centres and their surroundings. It is important to mention that we do not modify the total number of UFP_M concentrations per grid box in the following but that UFP_M concentrations are merely redistributed within each grid box.

Figure 9 illustrates the two-step downscaling procedure by the example of New Delhi and surroundings, using $PAE_{CEDS;0.5}$ to downscale to $0.5° \times 0.5°$ and $PAE_{EDGAR;0.1}$ for further downscaling, obtaining a UFP dataset with $0.1° \times 0.1°$ horizontal resolution. As a basis we calculate *relative anthropogenic emissions* (RAEs), i.e. the local anthropogenic particle number emissions relative to the average emissions of the grid box at coarser resolution:

$$RAE_{CEDS} = PAE_{CEDS;0.5}/PAE_{CEDS;GB},$$
$$RAE_{EDGAR} = PAE_{EDGAR;0.1}/PAE_{EDGAR;0.5}.$$

RAE_{CEDS} (top left in Fig. 9) and RAE_{EDGAR} (top right in Fig. 9) can be interpreted as the local excess or deficit of $PAE_{CEDS;0.5}$ ($PAE_{EDGAR;0.1}$) over $PAE_{CEDS;GB}$ ($PAE_{EDGAR;0.5}$), respectively. We limit RAE_{CEDS} to a maximum value of 10 and RAE_{EDGAR} to 7 due to missing observational datasets at locations with higher RAE.

In the first step we investigated the relationship between RAE_{CEDS} and the underestimation of UFP_O concentrations and PNC_O at each station (UFP_O / UFP_M or PNC_O / PNC_M) for all evaluation results in grid boxes with anthropogenic emissions exceeding two million particles per square metre and second.[2] The relationship is displayed in Fig. 8a. As expected, there is a logarithmic correlation ($r = 0.42$) between the two quantities. We perform a linear fit that crosses the

[2] All high-resolution pixels in the remaining (less anthropogenically influenced) grid boxes are bilinearly interpolated with respect to the coarser resolution.

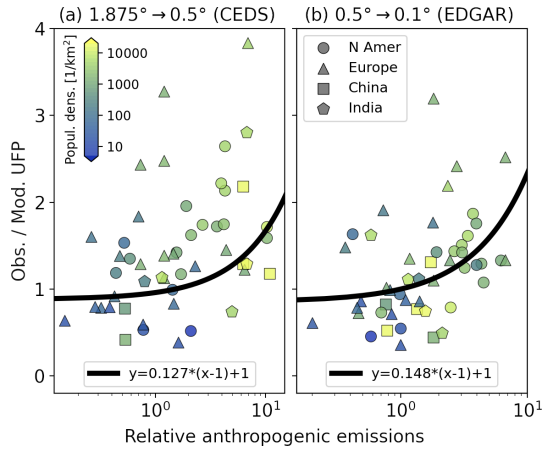

Figure 8. Scatterplot of the relative anthropogenic emissions (RAEs) against the model–measurement discrepancy (observed and simulated UFP concentrations). The RAEs of the CEDS database relative to the model grid box are directly compared to the model–measurement discrepancy **(a)**, while the RAEs of CEDS relative to the CEDS grid box are compared to the remaining discrepancy after the first downscaling **(b)**. We use the same colour code for the population density and shapes for the regions as in Fig. 7. The black lines show a linear fit crossing the (1,1) point. Higher RAEs correspond to a more pronounced underestimation of the observations.

point (1,1); i.e. $y = c_{\mathrm{CEDS}} \cdot (x-1)+1$, where y is the ratio $N_{\mathrm{obs}}/N_{\mathrm{mod}}$ and x is the $\mathrm{RAE}_{\mathrm{CEDS}}$. This function was chosen as it is the only global function that conserves the average grid box $\mathrm{UFP_M}$ concentrations after applying it to the model results. The fit parameter c was determined to be $c_{\mathrm{CEDS}} = 0.127$ using a logarithmic least squares fit. Thus, if $\mathrm{RAE_{CEDS}}$ increases by 1, the model underestimation increases by 0.127. The fit function is shown as a black line in Fig. 8a. This relationship is used to downscale simulated $\mathrm{UFP_M}$ concentrations, yielding redistributed UFP ($\mathrm{UFP_{0.5}}$) concentrations.

This procedure is repeated for the relationship between $\mathrm{RAE_{EDGAR}}$ and the remaining model–observation discrepancies after the first downscaling (Fig. 8b). We determine c_{EDGAR} to be $c = 0.148$, and thus $\mathrm{UFP_{0.5}}$ can be further downscaled to the urban and industrial environments, yielding redistributed $\mathrm{UFP_{0.1}}$ (hereafter referred to as $\mathrm{UFP_R}$) concentrations (rightmost plot in Fig. 9). Summarized, we obtain two downscaling functions that are applied sequentially to simulated $\mathrm{UFP_M}$ concentrations:

$$\mathrm{UFP_{0.5}} = \mathrm{UFP_M} \cdot (0.127 \cdot (\mathrm{RAE_{CEDS}} - 1) + 1),$$
$$\mathrm{UFP_R} = \mathrm{UFP_{0.5}} \cdot (0.148 \cdot (\mathrm{RAE_{EDGAR}} - 1) + 1).$$

To demonstrate the independence of the downscaling procedure from the data used for the fit, we randomly subdivided the non-remote measurement stations into a training and test dataset (25 for training, 24 for testing) in 5000 different random ways, derived the fit parameters from the training dataset only, and subsequently applied them to the test dataset. The results are displayed in Fig. 10. The fit parameters c_{CEDS} and c_{EDGAR} range between 0.07 and 0.23 in 90 % of the runs, while the average values are very close to the values derived from the complete dataset, and all derived fit parameters are greater than 0. The RMSLE consistently decreases with rising order of downscaling, with an average improvement of 0.11 in total (95.6 % of the time RMSLE decreases), while the logarithmic correlation increases on average by 0.07 (improves 95.1 % of the time). The bias $\overline{M/O}$ evolves from 0.78 on average in the model output resolution (2.4 % of the time between 0.9 and 1.1) to 0.92 after the CEDS downscaling (55.3 % of the time between 0.9 and 1.1) to 1.04 (66.2 % of the time between 0.9 and 1.1) after the final downscaling, slightly overestimating the observed values. We conclude that the fit parameters can be applied to data points outside the training dataset. However, as we want to maximize the number of measurement stations to use for the global downscaling, we use the complete evaluation results for the downscaling as described before.

The resulting $\mathrm{UFP_R}$ concentrations are included in Tables 1–5 in the last columns. At measurement sites in Europe, urban regions in the United States, India and China the agreement with measurements generally improves. For instance, $\mathrm{UFP_R}$ concentrations in Madrid, the measurement station with the strongest underestimation in this analysis (triangle in the top-right corner in Fig. 8a), are increased by a factor of 2.1, strongly improving the agreement (see Table 1: PF2 from 22 % to 59 %, $\overline{M/O}$ from 0.28 to 0.59). The remaining underestimation is likely caused by the influence of nearby roads with heavy traffic, which are of localized relevance only.

$\mathrm{UFP_R}$ in Beijing and Shanghai is strongly increased by the redistribution as well, which can even lead to an overestimation of the observed $\mathrm{UFP_O}$ concentrations (see Table 5). However, for Beijing the redistributed $\mathrm{UFP_R}$ falls between the high $\mathrm{UFP_O}$ from 2004–2006 and the lower $\mathrm{UFP_O}$ from 2018/19. This is in line with the emission reduction in China (see Sect. 4.1.4). $\mathrm{UFP_R}$ concentrations over Beijing's suburban Gucheng, sharing the model grid box with Beijing, are reduced, approaching $\mathrm{UFP_O}$ concentrations.

Similarly, $\mathrm{UFP_R}$ concentrations are strongly increased at the measurement stations Delhi IITM and Delhi IITD, resulting in $\mathrm{UFP_R}$ concentrations in between the two $\mathrm{UFP_O}$ concentrations. Moreover, $\mathrm{UFP_R}$ is only slightly increased at Delhi MRIU due to the lower local $\mathrm{PAE_{HR}}$, remaining similar to $\mathrm{UFP_O}$.

The left panel of Fig. 11 shows the comparison between $\mathrm{UFP_R}$ and $\mathrm{UFP_O}$ concentrations (analogously to Fig. 7) after the applied redistribution. In spite of the redistribution of UFPs within grid cells, there is still an overestimation of $\overline{M/O} = 1.27$ (1.32 before) at low population density below 100 individuals $\mathrm{km^{-2}}$. On the other hand, in densely populated regions (more than 1000 individuals $\mathrm{km^{-2}}$), simulated and observed UFP concentrations are of the same magnitude ($\overline{M/O} = 1.01$). Thus, the biases described in Sect. 4.1.6 are

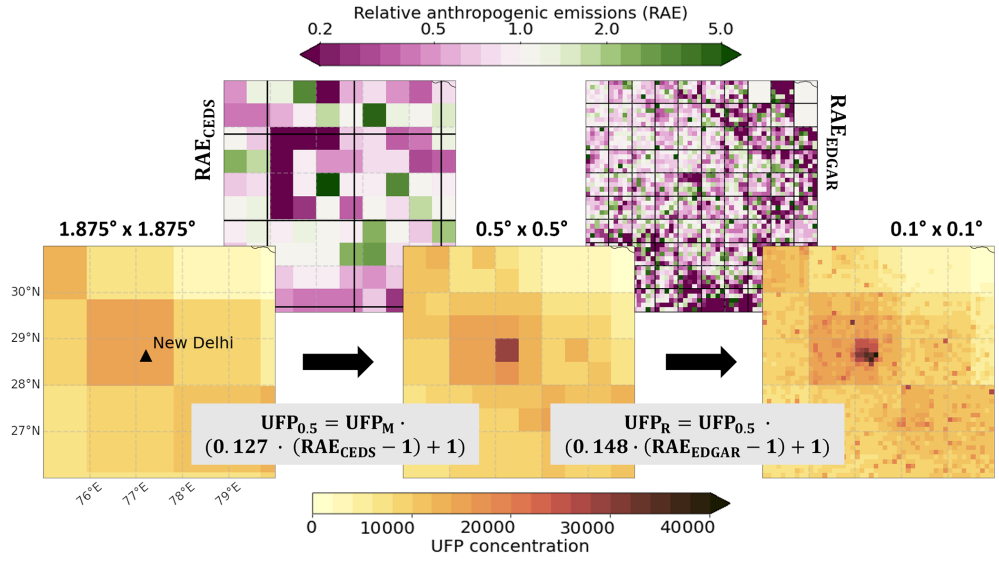

Figure 9. Illustration of the downscaling procedure using anthropogenic particle number emissions from the CEDS (Hoesly et al., 2018) and EDGAR (Crippa et al., 2022) emission databases, using the example of New Delhi and surroundings. Relative anthropogenic emissions (RAEs; local anthropogenic particle number emissions relative to the average over the initial grid box, displayed on the top) are set in relation to the model–observation discrepancy (observed and modelled UFP concentrations), displayed in Fig. 8. The resulting relation is used for downscaling UFP concentrations from the model resolution (1.875° × 1.875°) to 0.5° × 0.5° (CEDS) and 0.1° × 0.1° (EDGAR) horizontal resolutions in two steps. The average of the RAE over each grid box of the coarser resolution (black boxes) equals 1, and thus the respective average UFP concentrations per grid box remain unchanged. Note that the colour scale for UFP concentrations differs from Fig. 3.

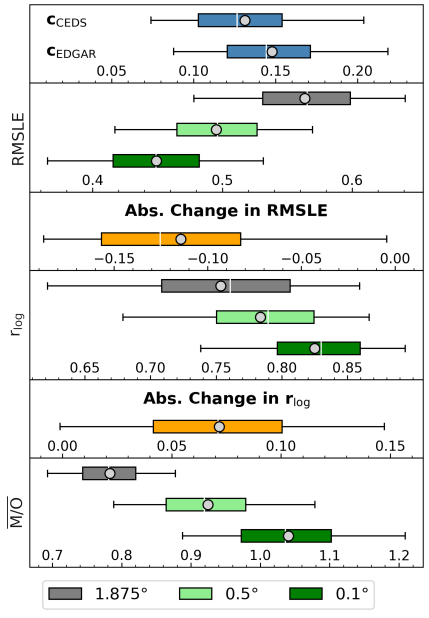

Figure 10. Results of 5000 independent training and test runs for the fit parameter estimation (25 stations in training dataset, 24 in test dataset). The fit parameters are displayed in the top panel, while the statistical measures are displayed below at different orders of downscaling, along with the absolute change in RMSLE and the logarithmic correlation. We show box-and-whisker plots, where the boxes illustrate the 25 %–75 % interval and the whiskers the 5 %–95 % interval. The median values are marked by the vertical white line and mean values by the light grey circles.

strongly reduced though not fully eliminated, especially for scarcely populated regions.

Evaluation results before and after the downscaling are displayed in the right panel of Fig. 11. The strong improvement in municipal regions is apparent when considering the urban measurement stations in the United States (top right), aligning closely around the centre line. An increase in correlation is also clearly visible in China, Europe and India.

All UFP_R concentrations differing by more than a factor of 2 from UFP_O can be attributed to nearby major traffic nodes and motorways (Leipzig-Eisenbahnstrasse) or alternatively coastal sites (Finokalia), a shielded location in a wheat field (Southern Great Plains E13) and the influence of a neighbouring megacity (Lin'an and Hyderabad). These discrepancies between UFP_R and UFP_O may perhaps be resolved with very high (< 1 km) horizontal resolution, which is computationally impracticable with a global model and cannot be achieved with downscaling due to missing emission datasets with respective horizontal resolution.

Finally, the logarithmic correlation between population density and UFP_R concentrations increases to $r = 0.77$ ($r = 0.57$ for UFP_M) after redistribution, which is similar to the logarithmic correlation between population density and UFP_O concentrations ($r = 0.80$). This indicates an improved representation of the anthropogenic influence in the downscaled dataset.

Figure 12 shows UFP_R concentrations in Asia after the applied downscaling, revealing more detailed features in

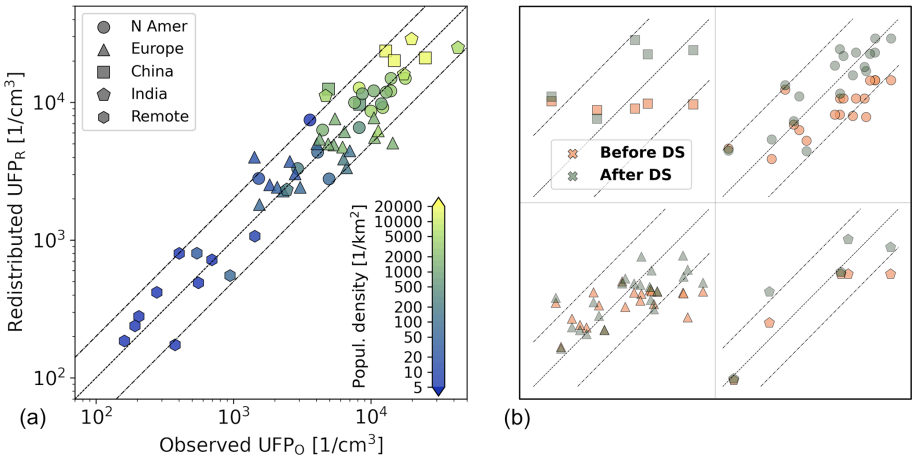

Figure 11. **(a)** The same as Fig. 7 but after the redistribution of UFP_M concentrations (downscaling) based on the relative anthropogenic emissions per grid box (more details in the text). **(b)** Evaluation results before and after the downscaling (DS) for China, North America, Europe and India (from top left to bottom right). Note that the value range differs in all subpanels.

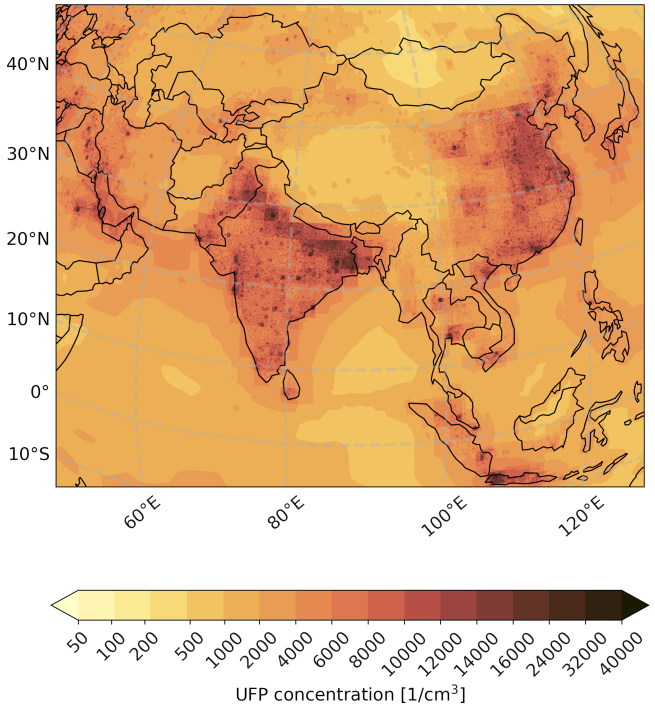

Figure 12. Annual average of UFP_R concentrations in Asia simulated with EMAC for the year 2015 after the downscaling based on primary anthropogenic emissions at a resolution of $0.1° \times 0.1°$. Note that the colour scale from Fig. 7 is extended as UFP_R concentrations can exceed 40 000 cm^{-3}.

anthropogenically influenced regions, especially in eastern China and northern India. Note that the colour scale is extended as UFP_R concentrations can exceed 40 000 cm^{-3} in Indian industrial regions, as well as in parts of urban environments in Mumbai, New Delhi, Shanghai, Riyadh, Kuwait and Cairo.

5 Limitations and uncertainties

As the resulting UFP_M and UFP_R concentrations are an intricate interplay of emission parameters, numerical simulation, evaluation and observation-guided redistribution, it is not possible to directly infer quantitative uncertainties for the provided datasets. However, the final results in Fig. 11 show that 90 % of the annually averaged UFP_R concentrations are within a factor of 2 of UFP_O concentrations (84 % for UFP_M), and all simulated UFP_R concentrations are within a factor of 3 of the observations after the emission-grid-based redistribution. Additional limitations and uncertainties are qualitatively discussed next.

Median diameters of directly emitted particles per sector were estimated based on the emission size distributions from Paasonen et al. (2016) and measurement reports in the literature with associated uncertainties. Additionally, we assumed the diameters to be globally identical for each sector and used the same diameters for all species. These simplifications lead to limitations in the precision by which the different sectors and species contribute to the total UFP_M and UFP_R number, respectively. Anthropogenic emissions are distributed in each time step based on monthly averages from the emission datasets. This potentially introduces bias due to the nonlinearity of chemical and microphysical processes. Future studies will include emission time factors to improve the time resolution of emissions.

Apart from UFP concentrations, we also used PNCs for the evaluation. PNCs are a proxy for UFP concentrations, as UFPs tend to dominate the total particle number (e.g. Baldauf et al., 2016; Kumar et al., 2014). However, locally there can be deviations. To increase the number of measurements for the evaluation we additionally used observations from years that differ from the simulation year (2015). Different meteorological conditions and emissions potentially lead to

biases in the evaluation. The downscaling was performed using evaluation results from differing years as well, while the simulation results were only taken from 2015. Thus, potential errors arise from the interference of the downscaling and general temporal trends, as seen from the analysis of the interannual variability in Sect. 4. The interannual variability (up to 50 % at low absolute UFP concentrations and below 20 % over polluted regions over a time span of 3 years) has been attributed to meteorological variations (along the ITCZ and mostly over the oceans) and decreasing (southern and eastern Asia, Europe, and the United States) or increasing (Nigeria and South Africa) long-term trends.

We define UFPs as all particles with a diameter smaller than 100 nm in the model without a lower cut on the particle diameter. Particles with a diameter below 1.7 nm are typically regarded as molecular clusters, and nucleation rates are reported as the frequency that clusters reach this threshold (e.g. by the CLOUD experiment; Kirkby et al., 2011). As a consequence, freshly formed particles are introduced to the model with a diameter of 1.7 nm. However, due to the lognormal modal aerosol distribution (Pringle et al., 2010), smaller particles down to infinitesimal small diameters are automatically created by definition. As a result, small fractions (up to around 2 % in polluted regions, with maximum values of up to 20 % locally over the oceans) of the presented UFPs have a diameter smaller than 1.7 nm. However, these particles are not considered to be molecular clusters as the low diameter is a result of computational effects.

In addition to the uncertainties introduced by the horizontal resolution of the model, the vertical resolution of the model, ranging from 45–70 m for the surface layer, adds additional uncertainties. While the surface layer is mostly entirely located in the boundary layer, decreases in UFP concentrations are still observed in general, as reported by Du et al. (2017), Harrison et al. (2019), Heintzenberg et al. (2011) and Villa et al. (2017), with the strongest decrease with altitude being observed close to UFP sources. We analysed the relative change in UFP concentrations from the surface layer to the next highest model level, exhibiting a decrease of 20 %–30 % in UFP concentrations on average over polluted regions, with the reduction slightly exceeding 50 % over central Africa. At higher latitudes, we even see increasing UFP concentrations at the second lowest model level. The decrease over polluted regions is in line with the observations from Du et al. (2017), Harrison et al. (2019) and Heintzenberg et al. (2011), who observe a decrease of up to 30 % at comparable altitudes.[3] Considering a linear decrease and increase within the range of 30 % within the model surface layer, this adds an additional uncertainty of ±15 % to the simulated UFP concentrations.

Finally, an important uncertainty is the spatio-temporal representativeness of the observations with respect to the model grid box and time sampling. We report three different types of representation errors:

1. purely spatial representation errors only due to the extent of the grid box at stations, for which timeline measurements of 2015 (mostly hourly) were available, and we collocated our simulation with the observations according to Schutgens et al. (2016b), i.e. all observations from the EBAS database;

2. spatio-temporal representation errors for measurement stations, for which only annual averages were available or the years differed from the evaluation year (2015); and

3. (spatio-)temporal representation errors for the aircraft measurements from ATom, for which we used daily averaged model output, and the measurement years differ from the simulation year. The spatial representation error is reduced by the fact that we have several measurements for each grid box.

The horizontal downscaling of UFP concentrations addresses and reduces the spatial representation error for types 1 and 2, while the temporal representation error of types 2 and 3 cannot be addressed.

The analysis in Sect. 4.2 showed that even after downscaling discrepancies in the evaluation remain, which are at least partly related to the representativeness of the measurement locations for the modelled grid areas (Schutgens et al., 2017, 2016a), also for UFP_R. Model concentrations of UFPs in rural regions in the vicinity of urban centres tend to be overestimated by the model (i.e. UFP_R). Hence, even for UFP_R the horizontal resolution is still a limiting factor. To further reduce the spatial representation error, the simulations would need to be performed at very high resolution requiring currently impracticable computing resources, at least for the global scale, as well as additional measurement data for UFPs and meteorological parameters in urban and industrialized regions including roadsides and background urban environments. Salma et al. (2014) showed that UFP concentrations can typically vary by a factor of 6 from the urban background to street canopies within cities, and Karner et al. (2010) showed that UFP concentrations reach (urban) background concentrations within about a kilometre. A next step could be to apply high-resolution dynamical downscaling of concentrations guided by comprehensive measurements of which data may become available in the future, using either machine learning methods or a combination of operational street pollution models and human exposure modelling as done by Ketzel et al. (2021). Clearly, to make progress, a much larger number of stations that continuously measure aerosol size distributions will need to be implemented.

[3] Villa et al. (2017) even observe a decrease of up to 80 %; however these measurements were performed directly at a highway and at some distance from other sources, which is not representative of a grid box covering approx. 180 × 180 km and overestimates the effect.

6 Conclusions

We presented the first numerical simulation of ultrafine particles (UFPs) at the Earth's surface with the global EMAC model, which includes a relatively detailed representation of aerosol formation and growth processes (i.e. the nucleation and Aitken aerosol size modes). Total concentrations were shown, along with interannual variability in the years 2015–2017 and the dominating particle size segments around the globe. Emissions of gaseous and aerosol species were taken from the CEDS and CAMS databases, and the emission radii for aerosol species were taken or derived from the literature referring to the contributing source sectors.

Simulated UFP and particle number concentrations (PNCs) were evaluated using particle size distributions and PNCs from field measurements, the EBAS database, literature, and published datasets. We generally achieve reasonable agreement between observed and simulated UFP concentrations, with good agreement for remote regions (forest, mountain, polar and ocean) that are not directly influenced by urban and other strong source regions (all simulated concentrations within a factor of 2 of the observations). In grid boxes with a high variance in population density, we obtain larger deviations with observations related to the coarse model resolution (approximately 180×180 km at the Equator). UFP concentrations in urban regions with a high population density are underestimated by the simulation, while they are overestimated in less densely populated regions. This representation error is associated with the high correlation between local population density and observed UFP concentrations (logarithmic correlation of $r = 0.80$) and is studied in depth by Schutgens et al. (2016a, b, 2017).

The relationship between the underestimation of the observed UFP concentrations and the local high-resolution anthropogenic emissions relative to the grid box average was used to redistribute UFPs within each grid box, leaving the total number of particles unchanged. This yields a higher resolution, i.e. downscaled data for grid boxes with dominant anthropogenic influence; increases the agreement between observations and simulations (the logarithmic correlation improves from 0.76 to 0.84 for non-remote regions and root mean squared logarithmic error from 0.57 to 0.43); and decreases the spatial representation error by improving the representation of the anthropogenic impact on UFP concentrations.

We provide two global annually averaged datasets of UFP concentrations for the year 2015 at different horizontal resolutions (https://doi.org/10.17617/3.7945XI, Kohl and Pozzer, 2023) that can be used for several purposes. The first dataset is given at a resolution of $1.875° \times 1.875°$ (roughly 180×180 km at the Equator) and is directly derived from the simulation. This dataset can serve the purpose of global-scale analyses of UFP concentrations, e.g. the comparison of different source regions, meteorology and atmospheric chemistry. The downscaled dataset has a much finer resolution of $0.1° \times 0.1°$ (roughly 10×10 km at the Equator and about 10×8 km at mid-latitudes) and includes the within-grid-box UFP redistribution based on anthropogenic emission data. The latter is recommended to be used to characterize the exposure to UFPs in public health studies with a focus on densely populated regions, in particular the urban environment. Additionally, we make the 2015 UFP concentrations available in three size bins (1.7–20, 20–50 and 50–100 nm).

Future applications may also include studies on seasonality, anthropogenic source sectors and the chemical composition of UFPs and their contribution to the health impacts of fine particulate matter.

Code availability. The Modular Earth Submodel System (MESSy) is continuously further developed and applied by a consortium of institutions. The usage of MESSy and access to the source code are licensed to all affiliates of institutions that are members of the MESSy Consortium. Institutions can become a member of the MESSy Consortium by signing the MESSy Memorandum of Understanding. More information can be found on the MESSy Consortium website (http://www.messy-interface.org, last access: 17 February 2023). The code presented here is available as git commit #49a7a544 in the MESSy repository, and all changes have been included in the main repository.

Scientific colour maps (https://doi.org/10.5281/zenodo.5501399, Crameri, 2021) are used in this study to prevent visual distortion of the data and exclusion of readers with colour vision deficiencies (Crameri et al., 2020).

Data availability. We provide datasets with annual averages of UFP concentrations for the year 2015, both in model resolution ($1.875° \times 1.875°$) directly derived from the model output, and at a resolution of $0.1° \times 0.1°$ with the observation-guided downscaling based on anthropogenic emissions. Additionally, we provide number concentrations in three size bins, i.e. 1.7–20, 20–50 and 50–100 nm. The datasets are publicly available at https://doi.org/10.17617/3.7945XI (Kohl and Pozzer, 2023).

Emission datasets from CEDS and EDGAR are available at https://doi.org/10.5281/zenodo.3754964 (McDuffie et al., 2020b) and https://edgar.jrc.ec.europa.eu/index.php/dataset_ap61 (Crippa et al., 2022), respectively. Emission size distributions are available at https://previous.iiasa.ac.at/web/home/research/researchPrograms/air/PN.html (Paasonen, 2016). Gridded Population of the World (v4) is taken from https://doi.org/10.7927/H4F47M65 (CIESIN, 2018). Measurement data from the ATom aircraft campaign are taken from https://doi.org/10.3334/ORNLDAAC/1671 (Brock et al., 2019).

Author contributions. SC, AP and JL planned the research. AP prepared the model set-up and performed the simulation with the help of MK and SC. DS, YC, SNT, MS, GP and HW helped in collecting and/or directly provided the observational datasets. SE developed the MESSy submodels NAN and IONS. MK analysed the model results, evaluated the simulation, developed the downscaling procedure and wrote the paper with the help of AP. JL and AP super-

vised the project. All authors discussed the results and contributed to the review and editing of the paper.

Competing interests. At least one of the (co-)authors is a member of the editorial board of *Atmospheric Chemistry and Physics*. The peer-review process was guided by an independent editor, and the authors also have no other competing interests to declare.

Disclaimer. Publisher's note: Copernicus Publications remains neutral with regard to jurisdictional claims made in the text, published maps, institutional affiliations, or any other geographical representation in this paper. While Copernicus Publications makes every effort to include appropriate place names, the final responsibility lies with the authors.

Special issue statement. This article is part of the special issue "The Modular Earth Submodel System (MESSy) (ACP/GMD interjournal SI)". It is not associated with a conference.

Acknowledgements. We acknowledge the work of Leslie Kremper, Marco Franco, Florian Ditas, Paulo Artaxo and Christopher Pöhlker, who collected and provided the observations at ATTO. We additionally acknowledge the effort of Chao Yan and Xiaojing Shen for providing the observational datasets from Beijing and Lin'an. The model simulations have been performed at the German Climate Computing Centre (DKRZ) through support from the Max Planck Society.

Financial support. This research has been supported by the Max Planck Graduate Center with the Johannes Gutenberg University (Mainz), the Science and Engineering Research Board, government of India (grant no. ECR/2016/001333), and the Institute of Eminence, University of Hyderabad (sanction no. UoH/IoE/RC1/RC1-20-014).

The article processing charges for this open-access publication were covered by the Max Planck Society.

Review statement. This paper was edited by Veli-Matti Kerminen and reviewed by two anonymous referees.

References

ACTRIS: ACTRIS Recommendation for mobility particle size spectrometer measurements, ACTRIS, https://www.actris-ecac.eu/pnsd-10-to-800nm.html (last access: 17 February 2023), 2021.

Amann, M., Bertok, I., Borken-Kleefeld, J., Cofala, J., Heyes, C., Höglund-Isaksson, L., Klimont, Z., Nguyen, B., Posch, M., Rafaj, P., Sandler, R., Schöpp, W., Wagner, F., and Winiwarter, W.: Cost-effective control of air quality and greenhouse gases in Europe: Modeling and policy applications, Environ. Model. Softw., 26, 1489–1501, https://doi.org/10.1016/j.envsoft.2011.07.012, 2011.

Andreae, M. O.: Correlation between cloud condensation nuclei concentration and aerosol optical thickness in remote and polluted regions, Atmos. Chem. Phys., 9, 543–556, https://doi.org/10.5194/acp-9-543-2009, 2009.

Andreae, M. O.: Emission of trace gases and aerosols from biomass burning – an updated assessment, Atmos. Chem. Phys., 19, 8523–8546, https://doi.org/10.5194/acp-19-8523-2019, 2019.

Andreae, M. O., Afchine, A., Albrecht, R., Holanda, B. A., Artaxo, P., Barbosa, H. M. J., Borrmann, S., Cecchini, M. A., Costa, A., Dollner, M., Fütterer, D., Järvinen, E., Jurkat, T., Klimach, T., Konemann, T., Knote, C., Krämer, M., Krisna, T., Machado, L. A. T., Mertes, S., Minikin, A., Pöhlker, C., Pöhlker, M. L., Pöschl, U., Rosenfeld, D., Sauer, D., Schlager, H., Schnaiter, M., Schneider, J., Schulz, C., Spanu, A., Sperling, V. B., Voigt, C., Walser, A., Wang, J., Weinzierl, B., Wendisch, M., and Ziereis, H.: Aerosol characteristics and particle production in the upper troposphere over the Amazon Basin, Atmos. Chem. Phys., 18, 921–961, https://doi.org/10.5194/acp-18-921-2018, 2018.

Baldauf, R. W., Devlin, R. B., Gehr, P., Giannelli, R., Hassett-Sipple, B., Jung, H., Martini, G., McDonald, J., Sacks, J. D., and Walker, K.: Ultrafine Particle Metrics and Research Considerations: Review of the 2015 UFP Workshop, Int. J. Environ. Res. Pu., 13, 1054, https://doi.org/10.3390/ijerph13111054, 2016.

Bellouin, N., Quaas, J., Gryspeerdt, E., Kinne, S., Stier, P., Watson-Parris, D., Boucher, O., Carslaw, K. S., Christensen, M., Daniau, A.-L., Dufresne, J.-L., Feingold, G., Fiedler, S., Forster, P., Gettelman, A., Haywood, J. M., Lohmann, U., Malavelle, F., Mauritsen, T., McCoy, D. T., Myhre, G., Mülmenstädt, J., Neubauer, D., Possner, A., Rugenstein, M., Sato, Y., Schulz, M., Schwartz, S. E., Sourdeval, O., Storelvmo, T., Toll, V., Winker, D., and Stevens, B.: Bounding Global Aerosol Radiative Forcing of Climate Change, Rev. Geophys., 58, e2019RG000660, https://doi.org/10.1029/2019RG000660, 2020.

Berrisford, P., Dee, D., Poli, P., Brugge, R., Fielding, M., Fuentes, M., Kållberg, P., Kobayashi, S., Uppala, S., and Simmons, A.: The ERA-Interim archive Version 2.0, Tech. Rep. 1, ECMWF, Shinfield Park, Reading, https://www.ecmwf.int/node/8174 (last access: 17 February 2023), 2011.

Brock, C., Kupc, A., Williamson, C., Froyd, K., Erdesz, F., Murphy, D., Schill, G., Gesler, D., MCLaughlin, R., Richardson, M., Wagner, N., and Wilson, J.: ATom: L2 In Situ Measurements of Aerosol Microphysical Properties (AMP), ORNL Distributed Active Archive Center [data set], https://doi.org/10.3334/ORNLDAAC/1671, 2019.

Burnett, R. T., Pope, C. A., Ezzati, M., Olives, C., Lim, S. S., Mehta, S., Shin, H. H., Singh, G., Hubbell, B., Brauer, M., Anderson, H. R., Smith, K. R., Balmes, J. R., Bruce, N. G., Kan, H., Laden, F., Prüss-Ustün, A., Turner, M. C., Gapstur, S. M., Diver, W. R., and Cohen, A.: An Integrated Risk Function for Estimating the Global Burden of Disease Attributable to Ambient Fine Particulate Matter Exposure, Environ. Health Persp., 122, 397–403, https://doi.org/10.1289/ehp.1307049, 2014.

CEN/TC 264/WG 32 – Air quality – Determination of the particle number concentration: CEN/TS 16976:2016: Ambient air – Determination of the particle number concentration of atmospheric aerosol, iTeh Stan-

dards, https://standards.iteh.ai/catalog/standards/cen/91f1ac67-f6d6-408c-af89-e81763194fd3/cen-ts-16976-2016 (last access: 17 February 2023), 2016.

CEN/TC 264/WG 32 – Air quality – Determination of the particle number concentration: CEN/TS 17434:2020: Ambient air – Determination of the particle number size distribution of atmospheric aerosol using a Mobility Particle Size Spectrometer (MPSS), iTeh Standards, https://standards.iteh.ai/catalog/standards/cen/a841bc08-ed34-4fa8-94ca-8c5e07b99db9/cen-ts-17434-2020 (last access: 17 February 2023), 2020.

Chen, X., Yu, F., Yang, W., Sun, Y., Chen, H., Du, W., Zhao, J., Wei, Y., Wei, L., Du, H., Wang, Z., Wu, Q., Li, J., An, J., and Wang, Z.: Global–regional nested simulation of particle number concentration by combing microphysical processes with an evolving organic aerosol module, Atmos. Chem. Phys., 21, 9343–9366, https://doi.org/10.5194/acp-21-9343-2021, 2021.

Chowdhury, S., Pozzer, A., Haines, A., Klingmüller, K., Münzel, T., Paasonen, P., Sharma, A., Venkataraman, C., and Lelieveld, J.: Global health burden of ambient $PM_{2.5}$ and the contribution of anthropogenic black carbon and organic aerosols, Environ. Int., 159, 107020, https://doi.org/10.1016/j.envint.2021.107020, 2022.

Christensen, M. W., Jones, W. K., and Stier, P.: Aerosols enhance cloud lifetime and brightness along the stratus-to-cumulus transition, P. Natl. Acad. Sci. USA, 117, 17591–17598, https://doi.org/10.1073/pnas.1921231117, 2020.

CIESIN (Center for International Earth Science Information Network): Gridded Population of the World, Version 4 (GPWv4): Population Density Adjusted to Match 2015 Revision UN WPP Country Totals, Revision 11, Center for International Earth Science Information Network [data set], https://doi.org/10.7927/H4F47M65, 2018.

Cohen, A. J., Ross Anderson, H., Ostro, B., Pandey, K. D., Krzyzanowski, M., Künzli, N., Gutschmidt, K., Pope, A., Romieu, I., Samet, J. M., and Smith, K.: The global burden of disease due to outdoor air pollution, J. Toxicol. Env. Heal. A, 68, 1301–1307, https://doi.org/10.1080/15287390590936166, 2005.

Crameri, F.: Scientific colour maps, Zenodo [code], https://doi.org/10.5281/zenodo.5501399, 2021.

Crameri, F., Shephard, G. E., and Heron, P. J.: The misuse of colour in science communication, Nat. Commun., 11, 1–10, https://doi.org/10.1038/s41467-020-19160-7, 2020.

Crippa, M., Solazzo, E., Huang, G., Guizzardi, D., Koffi, E., Muntean, M., Schieberle, C., Friedrich, R., and Janssens-Maenhout, G.: High resolution temporal profiles in the Emissions Database for Global Atmospheric Research, Scientific Data, 7, 1–17, https://doi.org/10.1038/s41597-020-0462-2, 2020.

Crippa, M., Guizzardi, D., Muntean, M., Schaaf, E., Monforti-Ferrario, F., Banja, M., Pagani, F., and Solazzo, E.: EDGAR v6.1 global air pollutant emissions, European Commission [data set], https://edgar.jrc.ec.europa.eu/index.php/dataset_ap61 (last access: 17 February 2023), 2022.

Curtius, J.: Nucleation of atmospheric aerosol particles, C. R. Phys., 7, 1027–1045, https://doi.org/10.1016/j.crhy.2006.10.018, 2006.

d'Almeida, G. A.: On the variability of desert aerosol radiative characteristics, J. Geophys. Res.-Atmos., 92, 3017–3026, https://doi.org/10.1029/JD092iD03p03017, 1987.

Delfino, R. J., Sioutas, C., and Malik, S.: Potential Role of Ultrafine Particles in Associations between Airborne Particle Mass and Cardiovascular Health, Environ. Health Persp., 113, 934–946, https://doi.org/10.1289/ehp.7938, 2005.

Dentener, F., Kinne, S., Bond, T., Boucher, O., Cofala, J., Generoso, S., Ginoux, P., Gong, S., Hoelzemann, J. J., Ito, A., Marelli, L., Penner, J. E., Putaud, J.-P., Textor, C., Schulz, M., van der Werf, G. R., and Wilson, J.: Emissions of primary aerosol and precursor gases in the years 2000 and 1750 prescribed data-sets for AeroCom, Atmos. Chem. Phys., 6, 4321–4344, https://doi.org/10.5194/acp-6-4321-2006, 2006.

Diesch, J.-M., Drewnick, F., Klimach, T., and Borrmann, S.: Investigation of gaseous and particulate emissions from various marine vessel types measured on the banks of the Elbe in Northern Germany, Atmos. Chem. Phys., 13, 3603–3618, https://doi.org/10.5194/acp-13-3603-2013, 2013.

Downward, G. S., van Nunen, E. J., Kerckhoffs, J., Vineis, P., Brunekreef, B., Boer, J. M., Messier, K. P., Roy, A., Verschuren, W. M. M., van der Schouw, Y. T., Sluijs, I., Gulliver, J., Hoek, G., and Vermeulen, R.: Long-term exposure to ultrafine particles and incidence of cardiovascular and cerebrovascular disease in a prospective study of a Dutch cohort, Environ. Health Persp., 126, 127007, https://doi.org/10.1289/EHP3047, 2018.

Du, W., Zhao, J., Wang, Y., Zhang, Y., Wang, Q., Xu, W., Chen, C., Han, T., Zhang, F., Li, Z., Fu, P., Li, J., Wang, Z., and Sun, Y.: Simultaneous measurements of particle number size distributions at ground level and 260 m on a meteorological tower in urban Beijing, China, Atmos. Chem. Phys., 17, 6797–6811, https://doi.org/10.5194/acp-17-6797-2017, 2017.

Dunne, E. M., Gordon, H., Kürten, A., Almeida, J., Duplissy, J., Williamson, C., Ortega, I. K., Pringle, K. J., Adamov, A., Baltensperger, U., Barmet, P., Benduhn, F., Bianchi, F., Breitenlechner, M., Clarke, A., Curtius, J., Dommen, J., Donahue, N. M., Ehrhart, S., Flagan, R. C., Franchin, A., Guida, R., Hakala, J., Hansel, A., Heinritzi, M., Jokinen, T., Kangasluoma, J., Kirkby, J., Kulmala, M., Kupc, A., Lawler, M. J., Lehtipalo, K., Makhmutov, V., Mann, G., Mathot, S., Merikanto, J., Miettinen, P., Nenes, A., Onnela, A., Rap, A., Reddington, C. L. S., Riccobono, F., Richards, N. A. D., Rissanen, M. P., Rondo, L., Sarnela, N., Schobesberger, S., Sengupta, K., Simon, M., Sipilä, M., Smith, J. N., Stozkhov, Y., Tomé, A., Tröstl, J., Wagner, P. E., Wimmer, D., Winkler, P. M., Worsnop, D. R., and Carslaw, K. S.: Global atmospheric particle formation from CERN CLOUD measurements, Science, 354, 1119–1124, https://doi.org/10.1126/science.aaf2649, 2016.

Ehrhart, S., Dunne, E. M., Manninen, H. E., Nieminen, T., Lelieveld, J., and Pozzer, A.: Two new submodels for the Modular Earth Submodel System (MESSy): New Aerosol Nucleation (NAN) and small ions (IONS) version 1.0, Geosci. Model Dev., 11, 4987–5001, https://doi.org/10.5194/gmd-11-4987-2018, 2018.

Fountoukis, C., Riipinen, I., Denier van der Gon, H. A. C., Charalampidis, P. E., Pilinis, C., Wiedensohler, A., O'Dowd, C., Putaud, J. P., Moerman, M., and Pandis, S. N.: Simulating ultrafine particle formation in Europe using a regional CTM: contribution of primary emissions versus secondary formation to aerosol number concentrations, Atmos. Chem. Phys., 12, 8663–8677, https://doi.org/10.5194/acp-12-8663-2012, 2012.

Franco, M. A., Ditas, F., Kremper, L. A., Machado, L. A. T., Andreae, M. O., Araújo, A., Barbosa, H. M. J., de Brito, J. F., Carbone, S., Holanda, B. A., Morais, F. G., Nascimento, J. P., Pöhlker, M. L., Rizzo, L. V., Sá, M., Saturno, J., Walter, D., Wolff, S., Pöschl, U., Artaxo, P., and Pöhlker, C.: Occurrence and growth of sub-50 nm aerosol particles in the Amazonian boundary layer, Atmos. Chem. Phys., 22, 3469–3492, https://doi.org/10.5194/acp-22-3469-2022, 2022.

Frohn, L. M., Ketzel, M., Christensen, J. H., Brandt, J., Im, U., Massling, A., Andersen, C., Plejdrup, M. S., Nielsen, O.-K., van der Gon, H. D., Manders-Groot, A., and Raaschou-Nielsen, O.: Modelling ultrafine particle number concentrations at address resolution in Denmark from 1979–2018 – Part 1: Regional and urban scale modelling and evaluation, Atmos. Environ., 264, 118631, https://doi.org/10.1016/j.atmosenv.2021.118631, 2021.

Gani, S., Bhandari, S., Patel, K., Seraj, S., Soni, P., Arub, Z., Habib, G., Hildebrandt Ruiz, L., and Apte, J. S.: Particle number concentrations and size distribution in a polluted megacity: the Delhi Aerosol Supersite study, Atmos. Chem. Phys., 20, 8533–8549, https://doi.org/10.5194/acp-20-8533-2020, 2020.

Gordon, H., Kirkby, J., Baltensperger, U., Bianchi, F., Breitenlechner, M., Curtius, J., Dias, A., Dommen, J., Donahue, N. M., Dunne, E. M., Duplissy, J., Ehrhart, S., Flagan, R. C., Frege, C., Fuchs, C., Hansel, A., Hoyle, C. R., Kulmala, M., Kürten, A., Lehtipalo, K., Makhmutov, V., Molteni, U., Rissanen, M. P., Stozkhov, Y., Tröstl, J., Tsagkogeorgas, G., Wagner, R., Williamson, C., Wimmer, D., Winkler, P. M., Yan, C., and Carslaw, K. S.: Causes and importance of new particle formation in the present-day and preindustrial atmospheres, J. Geophys. Res.-Atmos., 122, 8739–8760, https://doi.org/10.1002/2017JD026844, 2017.

Granier, C., Darras, S., Denier van der Gon, H., Doubalova, J., Elguindi, N., Galle, B., Gauss, M., Guevara, M., Jalkanen, J.-P., Kuenen, J., Liousse, C., Quack, B., Simpson, D., and Sindelarova, K.: The Copernicus Atmosphere Monitoring Service global and regional emissions (April 2019 version), Copernicus Atmosphere Monitoring Service (CAMS) report, https://doi.org/10.24380/d0bn-kx16, 2019.

Guelle, W., Schulz, M., Balkanski, Y., and Dentener, F.: Influence of the source formulation on modeling the atmospheric global distribution of sea salt aerosol, J. Geophys. Res.-Atmos., 106, 27509–27524, https://doi.org/10.1029/2001JD900249, 2001.

Harrison, R. M., Beddows, D. C. S., Alam, M. S., Singh, A., Brean, J., Xu, R., Kotthaus, S., and Grimmond, S.: Interpretation of particle number size distributions measured across an urban area during the FASTER campaign, Atmos. Chem. Phys., 19, 39–55, https://doi.org/10.5194/acp-19-39-2019, 2019.

Heintzenberg, J., Birmili, W., Otto, R., Andreae, M. O., Mayer, J.-C., Chi, X., and Panov, A.: Aerosol particle number size distributions and particulate light absorption at the ZOTTO tall tower (Siberia), 2006–2009, Atmos. Chem. Phys., 11, 8703–8719, https://doi.org/10.5194/acp-11-8703-2011, 2011.

Hoesly, R. M., Smith, S. J., Feng, L., Klimont, Z., Janssens-Maenhout, G., Pitkanen, T., Seibert, J. J., Vu, L., Andres, R. J., Bolt, R. M., Bond, T. C., Dawidowski, L., Kholod, N., Kurokawa, J.-I., Li, M., Liu, L., Lu, Z., Moura, M. C. P., O'Rourke, P. R., and Zhang, Q.: Historical (1750–2014) anthropogenic emissions of reactive gases and aerosols from the Community Emissions Data System (CEDS), Geosci. Model Dev., 11, 369–408, https://doi.org/10.5194/gmd-11-369-2018, 2018.

Hong, G. and Jee, Y.-K.: Special issue on ultrafine particles: where are they from and how do they affect us?, Exp. Mol. Med., 52, 309–310, https://doi.org/10.1038/s12276-020-0395-z, 2020.

Janhäll, S., Andreae, M. O., and Pöschl, U.: Biomass burning aerosol emissions from vegetation fires: particle number and mass emission factors and size distributions, Atmos. Chem. Phys., 10, 1427–1439, https://doi.org/10.5194/acp-10-1427-2010, 2010.

Jeuken, A. B. M., Siegmund, P. C., Heijboer, L. C., Feichter, J., and Bengtsson, L.: On the potential of assimilating meteorological analyses in a global climate model for the purpose of model validation, J. Geophys. Res.-Atmos., 101, 16939–16950, https://doi.org/10.1029/96JD01218, 1996.

Jöckel, P., Tost, H., Pozzer, A., Brühl, C., Buchholz, J., Ganzeveld, L., Hoor, P., Kerkweg, A., Lawrence, M. G., Sander, R., Steil, B., Stiller, G., Tanarhte, M., Taraborrelli, D., van Aardenne, J., and Lelieveld, J.: The atmospheric chemistry general circulation model ECHAM5/MESSy1: consistent simulation of ozone from the surface to the mesosphere, Atmos. Chem. Phys., 6, 5067–5104, https://doi.org/10.5194/acp-6-5067-2006, 2006.

Jöckel, P., Kerkweg, A., Pozzer, A., Sander, R., Tost, H., Riede, H., Baumgaertner, A., Gromov, S., and Kern, B.: Development cycle 2 of the Modular Earth Submodel System (MESSy2), Geosci. Model Dev., 3, 717–752, https://doi.org/10.5194/gmd-3-717-2010, 2010.

Karner, A. A., Eisinger, D. S., and Niemeier, D. A.: Near-Roadway Air Quality: Synthesizing the Findings from Real-World Data, Environ. Sci. Technol., 44, 5334–5344, https://doi.org/10.1021/es100008x, 2010.

Kasper, A., Aufdenblatten, S., Forss, A., Mohr, M., and Burtscher, H.: Particulate Emissions from a Low-Speed Marine Diesel Engine, Aerosol Sci. Tech., 41, 24–32, https://doi.org/10.1080/02786820601055392, 2007.

Kerkweg, A., Sander, R., Tost, H., and Jöckel, P.: Technical note: Implementation of prescribed (OFFLEM), calculated (ONLEM), and pseudo-emissions (TNUDGE) of chemical species in the Modular Earth Submodel System (MESSy), Atmos. Chem. Phys., 6, 3603–3609, https://doi.org/10.5194/acp-6-3603-2006, 2006.

Ketzel, M., Frohn, L. M., Christensen, J. H., Brandt, J., Massling, A., Andersen, C., Im, U., Jensen, S. S., Khan, J., Nielsen, O.-K., Plejdrup, M. S., Manders, A., van der Gon, H. D., Kumar, P., and Raaschou-Nielsen, O.: Modelling ultrafine particle number concentrations at address resolution in Denmark from 1979 to 2018 – Part 2: Local and street scale modelling and evaluation, Atmos. Environ., 264, 118633, https://doi.org/10.1016/j.atmosenv.2021.118633, 2021.

Kohl, M. and Pozzer, A.: Simulated global ultrafine particle (UFP) concentrations, Edmond, V1 [data set], https://doi.org/10.17617/3.7945XI, 2023.

Kirkby, J., Curtius, J., Almeida, J., Dunne, E., Duplissy, J., Ehrhart, S., Franchin, A., Gagné, S., Ickes, L., Kürten, A., Kupc, A., Metzger, A., Riccobono, F., Rondo, L., Schobesberger, G. T., Tsagkogeorgas, G., Wimmer, D., Amorim, A., Bianchi, F., Breitenlechner, M., David, A., Dommen, J., Downard, A., Ehn, M., Flagan, R. C., Haider, S., Hansel, A., Hauser, D., Jud, W., Junninen, H., Kreissl, F., Kvashin, A., Laaksonen, A., Lehtipalo, K.,

Lima, J., Lovejoy, E. R., Makhmutov, V., Mathot, S., Mikkilä, J., Minginette, P., Mogo, S., Nieminen, T., Onnela, A., Pereira, P., Petaja, T., Schnitzhofer, R., Seinfeld, J., Sipila, M., Stozhkov, Y., Stratmann, F., Tome, A., Vanhanen, J., Viisanen, Y., Vrtala, A., Wagner, P., Walther, H., Weingartner, E., Wex, H., Winkler, P., Carslaw, K., Worsnop, D., Baltensperger, U., and Kulmala, M.: Role of sulphuric acid, ammonia and galactic cosmic rays in atmospheric aerosol nucleation, Nature, 476, 429–433, https://doi.org/10.1038/nature10343, 2011.

Kirkby, J., Duplissy, J., Sengupta, K., Frege, C., Gordon, H., Williamson, C., Heinritzi, M., Simon, M., Yan, C., Almeida, J., Tröstl, J., Nieminen, T., Ortega, I. K., Wagner, R., Adamov, A., Amorim, A., Bernhammer, A.-K., Bianchi, F., Breitenlechner, M., Brilke, S., Chen, X., Craven, J., Dias, A., Ehrhart, S., Flagan, R. C., Franchin, A., Fuchs, C., Guida, R., Hakala, J., Hoyle, C. R., Jokinen, T., Junninen, H., Kangasluoma, J., Kim, J., Krapf, M., Kürten, A., Laaksonen, A., Lehtipalo, K., Makhmutov, V., Mathot, S., Molteni, U., Onnela, A., Peräkylä, O., Piel, F., Petäjä, T., Praplan, A. P., Pringle, K., Rap, A., Richards, N. A. D., Riipinen, I., Rissanen, M. P., Rondo, L., Sarnela, N., Schobesberger, S., Scott, C. E., Seinfeld, J. H., Sipilä, M., Steiner, G., Stozhkov, Y., Stratmann, F., Tomé, A., Virtanen, A., Vogel, A. L., Wagner, A. C., Wagner, P. E., Weingartner, E., Wimmer, D., Winkler, P. M., Ye, P., Zhang, X., Hansel, A., Dommen, J., Donahue, N. M., Worsnop, D. R., Baltensperger, U., Kulmala, M., Carslaw, K. S., and Curtius, J.: Ion-induced nucleation of pure biogenic particles, Nature, 533, 521–526, https://doi.org/10.1038/nature17953, 2016.

Klingmüller, K., Metzger, S., Abdelkader, M., Karydis, V. A., Stenchikov, G. L., Pozzer, A., and Lelieveld, J.: Revised mineral dust emissions in the atmospheric chemistry–climate model EMAC (MESSy 2.52 DU_Astitha1 KKDU2017 patch), Geosci. Model Dev., 11, 989–1008, https://doi.org/10.5194/gmd-11-989-2018, 2018.

Kukkonen, J., Karl, M., Keuken, M. P., Denier van der Gon, H. A. C., Denby, B. R., Singh, V., Douros, J., Manders, A., Samaras, Z., Moussiopoulos, N., Jonkers, S., Aarnio, M., Karppinen, A., Kangas, L., Lützenkirchen, S., Petäjä, T., Vouitsis, I., and Sokhi, R. S.: Modelling the dispersion of particle numbers in five European cities, Geosci. Model Dev., 9, 451–478, https://doi.org/10.5194/gmd-9-451-2016, 2016.

Kulmala, M., Vehkamäki, H., Petäjä, T., Dal Maso, M., Lauri, A., Kerminen, V.-M., Birmili, W., and McMurry, P.: Formation and growth rates of ultrafine atmospheric particles: a review of observations, J. Aerosol Sci., 35, 143–176, https://doi.org/10.1016/j.jaerosci.2003.10.003, 2004.

Kumar, P., Morawska, L., Birmili, W., Paasonen, P., Hu, M., Kulmala, M., Harrison, R. M., Norford, L., and Britter, R.: Ultrafine particles in cities, Environ. Int., 66, 1–10, https://doi.org/10.1016/j.envint.2014.01.013, 2014.

Kwon, H.-S., Ryu, M. H., and Carlsten, C.: Ultrafine particles: unique physicochemical properties relevant to health and disease, Exp. Mol. Med., 52, 318–328, https://doi.org/10.1038/s12276-020-0405-1, 2020.

Lelieveld, J., Evans, J. S., Fnais, M., Giannadaki, D., and Pozzer, A.: The contribution of outdoor air pollution sources to premature mortality on a global scale, Nature, 525, 367–371, https://doi.org/10.1038/nature15371, 2015.

Lelieveld, J., Klingmüller, K., Pozzer, A., Burnett, R. T., Haines, A., and Ramanathan, V.: Effects of fossil fuel and total anthropogenic emission removal on public health and climate, P. Natl. Acad. Sci. USA, 116, 7192–7197, https://doi.org/10.1073/pnas.1819989116, 2019.

Lelieveld, J., Pozzer, A., Pöschl, U., Fnais, M., Haines, A., and Münzel, T.: Loss of life expectancy from air pollution compared to other risk factors: a worldwide perspective, Cardiovasc. Res., 116, 1910–1917, https://doi.org/10.1093/cvr/cvaa025, 2020.

Li, G., Su, H., Ma, N., Tao, J., Kuang, Y., Wang, Q., Hong, J., Zhang, Y., Kuhn, U., Zhang, S., Pan, X., Lu, N., Tang, M., Zheng, G., Wang, Z., Gao, Y., Cheng, P., Xu, W., Zhou, G., Zhao, C., Yuan, B., Shao, M., Ding, A., Zhang, Q., Fu, P., Sun, Y., Pöschl, U., and Cheng, Y.: Multiphase chemistry experiment in Fogs and Aerosols in the North China Plain (McFAN): integrated analysis and intensive winter campaign 2018, Faraday Discuss., 226, 207–222, https://doi.org/10.1039/D0FD00099J, 2021.

Liu, M. and Matsui, H.: Secondary Organic Aerosol Formation Regulates Cloud Condensation Nuclei in the Global Remote Troposphere, Geophys. Res. Lett., 49, e2022GL100543, https://doi.org/10.1029/2022GL100543, 2022.

Liu, Y., Yan, C., Feng, Z., Zheng, F., Fan, X., Zhang, Y., Li, C., Zhou, Y., Lin, Z., Guo, Y., Zhang, Y., Ma, L., Zhou, W., Liu, Z., Dada, L., Dällenbach, K., Kontkanen, J., Cai, R., Chan, T., Chu, B., Du, W., Yao, L., Wang, Y., Cai, J., Kangasluoma, J., Kokkonen, T., Kujansuu, J., Rusanen, A., Deng, C., Fu, Y., Yin, R., Li, X., Lu, Y., Liu, Y., Lian, C., Yang, D., Wang, W., Ge, M., Wang, Y., Worsnop, D. R., Junninen, H., He, H., Kerminen, V.-M., Zheng, J., Wang, L., Jiang, J., Petäjä, T., Bianchi, F., and Kulmala, M.: Continuous and comprehensive atmospheric observations in Beijing: a station to understand the complex urban atmospheric environment, Big Earth Data, 4, 295–321, https://doi.org/10.1080/20964471.2020.1798707, 2020.

Lohmann, U. and Feichter, J.: Global indirect aerosol effects: a review, Atmos. Chem. Phys., 5, 715–737, https://doi.org/10.5194/acp-5-715-2005, 2005.

Lu, X., Zhang, S., Xing, J., Wang, Y., Chen, W., Ding, D., Wu, Y., Wang, S., Duan, L., and Hao, J.: Progress of Air Pollution Control in China and Its Challenges and Opportunities in the Ecological Civilization Era, Engineering, 6, 1423–1431, https://doi.org/10.1016/j.eng.2020.03.014, 2020.

McDuffie, E. E., Smith, S. J., O'Rourke, P., Tibrewal, K., Venkataraman, C., Marais, E. A., Zheng, B., Crippa, M., Brauer, M., and Martin, R. V.: A global anthropogenic emission inventory of atmospheric pollutants from sector- and fuel-specific sources (1970–2017): an application of the Community Emissions Data System (CEDS), Earth Syst. Sci. Data, 12, 3413–3442, https://doi.org/10.5194/essd-12-3413-2020, 2020a.

McDuffie, E., Smith, S., O'Rourke, P., Tibrewal, K., Venkataraman, C., Marais, E., Zheng, B., Crippa, M., Brauer, M., and Martin, R.: CEDS_GBD-MAPS: Global Anthropogenic Emission Inventory of NOx, SO2, CO, NH3, NMVOCs, BC, and OC from 1970–2017 (2020_v1.0), Zenodo [data set], https://doi.org/10.5281/zenodo.3754964, 2020b.

Monahan, E. C.: The Ocean as a Source for Atmospheric Particles, Springer Netherlands, Dordrecht, 129–163, https://doi.org/10.1007/978-94-009-4738-2_6, 1986.

Murray, C. J., Aravkin, A. Y., Zheng, P., et al.: Global burden of 87 risk factors in 204 countries and territories, 1990–2019:

a systematic analysis for the Global Burden of Disease Study 2019, Lancet, 396, 1223–1249, https://doi.org/10.1016/S0140-6736(20)30752-2, 2020.

Paasonen, P.: Global particle number emissions, International Institute for Applied System Analysis [data set], https://previous.iiasa.ac.at/web/home/research/researchPrograms/air/PN.html (last access: 17 February 2023), 2016.

Paasonen, P., Kupiainen, K., Klimont, Z., Visschedijk, A., Denier van der Gon, H. A. C., and Amann, M.: Continental anthropogenic primary particle number emissions, Atmos. Chem. Phys., 16, 6823–6840, https://doi.org/10.5194/acp-16-6823-2016, 2016.

Pan, X., Ichoku, C., Chin, M., Bian, H., Darmenov, A., Colarco, P., Ellison, L., Kucsera, T., da Silva, A., Wang, J., Oda, T., and Cui, G.: Six global biomass burning emission datasets: intercomparison and application in one global aerosol model, Atmos. Chem. Phys., 20, 969–994, https://doi.org/10.5194/acp-20-969-2020, 2020.

Petzold, A. and Schröder, F. P.: Jet Engine Exhaust Aerosol Characterization, Aerosol Sci. Tech., 28, 62–76, https://doi.org/10.1080/02786829808965512, 1998.

Petzold, A., Stein, C., Nyeki, S., Gysel, M., Weingartner, E., Baltensperger, U., Giebl, H., Hitzenberger, R., Döpelheuer, A., Vrchoticky, S., Puxbaum, H., Johnson, M., Hurley, C. D., Marsh, R., and Wilson, C. W.: Properties of jet engine combustion particles during the PartEmis experiment: Microphysics and Chemistry, Geophys. Res. Lett., 30, 1719, https://doi.org/10.1029/2003GL017283, 2003.

Petzold, A., Hasselbach, J., Lauer, P., Baumann, R., Franke, K., Gurk, C., Schlager, H., and Weingartner, E.: Experimental studies on particle emissions from cruising ship, their characteristic properties, transformation and atmospheric lifetime in the marine boundary layer, Atmos. Chem. Phys., 8, 2387–2403, https://doi.org/10.5194/acp-8-2387-2008, 2008.

Pope, C. A. and Dockery, D. W.: Health Effects of Fine Particulate Air Pollution: Lines that Connect, J. Air Waste Manage. Assoc., 56, 709–742, https://doi.org/10.1080/10473289.2006.10464485, 2006.

Pöschl, U., von Kuhlmann, R., Poisson, N., and Crutzen, P. J.: Development and intercomparison of condensed isoprene oxidation mechanisms for global atmospheric modeling, J. Atmos. Chem., 37, 29–52, https://doi.org/10.1023/A:1006391009798, 2000.

Pozzer, A., Jöckel, P., and Van Aardenne, J.: The influence of the vertical distribution of emissions on tropospheric chemistry, Atmos. Chem. Phys., 9, 9417–9432, https://doi.org/10.5194/acp-9-9417-2009, 2009.

Pozzer, A., de Meij, A., Pringle, K. J., Tost, H., Doering, U. M., van Aardenne, J., and Lelieveld, J.: Distributions and regional budgets of aerosols and their precursors simulated with the EMAC chemistry-climate model, Atmos. Chem. Phys., 12, 961–987, https://doi.org/10.5194/acp-12-961-2012, 2012.

Pozzer, A., de Meij, A., Yoon, J., Tost, H., Georgoulias, A. K., and Astitha, M.: AOD trends during 2001–2010 from observations and model simulations, Atmos. Chem. Phys., 15, 5521–5535, https://doi.org/10.5194/acp-15-5521-2015, 2015.

Pozzer, A., Reifenberg, S. F., Kumar, V., Franco, B., Kohl, M., Taraborrelli, D., Gromov, S., Ehrhart, S., Jöckel, P., Sander, R., Fall, V., Rosanka, S., Karydis, V., Akritidis, D., Emmerichs, T., Crippa, M., Guizzardi, D., Kaiser, J. W., Clarisse, L., Kiendler-Scharr, A., Tost, H., and Tsimpidi, A.: Simulation of organics in the atmosphere: evaluation of EMACv2.54 with the Mainz Organic Mechanism (MOM) coupled to the ORACLE (v1.0) submodel, Geosci. Model Dev., 15, 2673–2710, https://doi.org/10.5194/gmd-15-2673-2022, 2022.

Pringle, K. J., Tost, H., Message, S., Steil, B., Giannadaki, D., Nenes, A., Fountoukis, C., Stier, P., Vignati, E., and Lelieveld, J.: Description and evaluation of GMXe: a new aerosol submodel for global simulations (v1), Geosci. Model Dev., 3, 391–412, https://doi.org/10.5194/gmd-3-391-2010, 2010.

Reid, J. S., Koppmann, R., Eck, T. F., and Eleuterio, D. P.: A review of biomass burning emissions part II: intensive physical properties of biomass burning particles, Atmos. Chem. Phys., 5, 799–825, https://doi.org/10.5194/acp-5-799-2005, 2005.

Riccobono, F., Schobesberger, S., Scott, C. E., Dommen, J., Ortega, I. K., Rondo, L., Almeida, J., Amorim, A., Bianchi, F., Breitenlechner, M., David, A., Downard, A., Dunne, E. M., Duplissy, J., Ehrhart, S., Flagan, R. C., Franchin, A., Hansel, A., Junninen, H., Kajos, M., Keskinen, H., Kupc, A., Kürten, A., Kvashin, A. N., Laaksonen, A., Lehtipalo, K., Makhmutov, V., Mathot, S., Nieminen, T., Onnela, A., Petäjä, T., Praplan, A. P., Santos, F. D., Schallhart, S., Seinfeld, J. H., Sipilä, M., Spracklen, D. V., Stozhkov, Y., Stratmann, F., Tomé, A., Tsagkogeorgas, G., Vaattovaara, P., Viisanen, Y., Vrtala, A., Wagner, P. E., Weingartner, E., Wex, H., Wimmer, D., Carslaw, K. S., Curtius, J., Donahue, N. M., Kirkby, J., Kulmala, M., Worsnop, D. R., and Baltensperger, U.: Oxidation Products of Biogenic Emissions Contribute to Nucleation of Atmospheric Particles, Science, 344, 717–721, https://doi.org/10.1126/science.1243527, 2014.

Roeckner, E., Bäuml, G., Bonaventura, L., Brokopf, R., Esch, M., Giorgetta, M., Hagemann, S., Kirchner, I., Kornblueh, L., Manzini, E., Hagemann, S., Kirchner, I., Kornblueh, L., Manzini, E., Schlese, U., and Schulzweida, U.: The atmospheric general circulation model ECHAM 5. PART I: Model description, Tech. rep., Max-Planck-Institut für Meteorologie, https://doi.org/10.17617/2.995269, 2003.

Rose, C., Collaud Coen, M., Andrews, E., Lin, Y., Bossert, I., Lund Myhre, C., Tuch, T., Wiedensohler, A., Fiebig, M., Aalto, P., Alastuey, A., Alonso-Blanco, E., Andrade, M., Artíñano, B., Arsov, T., Baltensperger, U., Bastian, S., Bath, O., Beukes, J. P., Brem, B. T., Bukowiecki, N., Casquero-Vera, J. A., Conil, S., Eleftheriadis, K., Favez, O., Flentje, H., Gini, M. I., Gómez-Moreno, F. J., Gysel-Beer, M., Hallar, A. G., Kalapov, I., Kalivitis, N., Kasper-Giebl, A., Keywood, M., Kim, J. E., Kim, S.-W., Kristensson, A., Kulmala, M., Lihavainen, H., Lin, N.-H., Lyamani, H., Marinoni, A., Martins Dos Santos, S., Mayol-Bracero, O. L., Meinhardt, F., Merkel, M., Metzger, J.-M., Mihalopoulos, N., Ondracek, J., Pandolfi, M., Pérez, N., Petäjä, T., Petit, J.-E., Picard, D., Pichon, J.-M., Pont, V., Putaud, J.-P., Reisen, F., Sellegri, K., Sharma, S., Schauer, G., Sheridan, P., Sherman, J. P., Schwerin, A., Sohmer, R., Sorribas, M., Sun, J., Tulet, P., Vakkari, V., van Zyl, P. G., Velarde, F., Villani, P., Vratolis, S., Wagner, Z., Wang, S.-H., Weinhold, K., Weller, R., Yela, M., Zdimal, V., and Laj, P.: Seasonality of the particle number concentration and size distribution: a global analysis retrieved from the network of Global Atmosphere Watch (GAW) near-surface observatories, Atmos. Chem. Phys., 21, 17185–17223, https://doi.org/10.5194/acp-21-17185-2021, 2021.

Saha, P. K., Hankey, S., Marshall, J. D., Robinson, A. L., and Presto, A. A.: High-Spatial-Resolution Estimates of Ultrafine Particle Concentrations across the Continental United States, Environ. Sci. Technol., 55, 10320–10331, https://doi.org/10.1021/acs.est.1c03237, 2021.

Salma, I., Borsós, T., Németh, Z., Weidinger, T., Aalto, P., and Kulmala, M.: Comparative study of ultrafine atmospheric aerosol within a city, Atmos. Environ., 92, 154–161, https://doi.org/10.1016/j.atmosenv.2014.04.020, 2014.

Sander, R., Baumgaertner, A., Cabrera-Perez, D., Frank, F., Gromov, S., Grooß, J.-U., Harder, H., Huijnen, V., Jöckel, P., Karydis, V. A., Niemeyer, K. E., Pozzer, A., Riede, H., Schultz, M. G., Taraborrelli, D., and Tauer, S.: The community atmospheric chemistry box model CAABA/MECCA-4.0, Geosci. Model Dev., 12, 1365–1385, https://doi.org/10.5194/gmd-12-1365-2019, 2019.

Schraufnagel, D. E.: The health effects of ultrafine particles, Exp. Mol. Med., 52, 311–317, https://doi.org/10.1038/s12276-020-0403-3, 2020.

Schraufnagel, D. E., Balmes, J. R., Cowl, C. T., De Matteis, S., Jung, S.-H., Mortimer, K., Perez-Padilla, R., Rice, M. B., Riojas-Rodriguez, H., Sood, A., Thurston, G. D., To, T., Vanker, A., and Wuebbles, D. J.: Air Pollution and Noncommunicable Diseases: A Review by the Forum of International Respiratory Societies' Environmental Committee, Part 2: Air Pollution and Organ Systems, Chest, 155, 417–426, https://doi.org/10.1016/j.chest.2018.10.041, 2019.

Schutgens, N. A. J., Gryspeerdt, E., Weigum, N., Tsyro, S., Goto, D., Schulz, M., and Stier, P.: Will a perfect model agree with perfect observations? The impact of spatial sampling, Atmos. Chem. Phys., 16, 6335–6353, https://doi.org/10.5194/acp-16-6335-2016, 2016a.

Schutgens, N. A. J., Partridge, D. G., and Stier, P.: The importance of temporal collocation for the evaluation of aerosol models with observations, Atmos. Chem. Phys., 16, 1065–1079, https://doi.org/10.5194/acp-16-1065-2016, 2016b.

Schutgens, N., Tsyro, S., Gryspeerdt, E., Goto, D., Weigum, N., Schulz, M., and Stier, P.: On the spatio-temporal representativeness of observations, Atmos. Chem. Phys., 17, 9761–9780, https://doi.org/10.5194/acp-17-9761-2017, 2017.

Sebastian, M., Kompalli, S. K., Kumar, V. A., Jose, S., Babu, S. S., Pandithurai, G., Singh, S., Hooda, R. K., Soni, V. K., Pierce, J. R., Vakkari, V., Asmi, E., Westervelt, D. M., Hyvärinen, A.-P., and Kanawade, V. P.: Observations of particle number size distributions and new particle formation in six Indian locations, Atmos. Chem. Phys., 22, 4491–4508, https://doi.org/10.5194/acp-22-4491-2022, 2022.

Seinfeld, J. H. and Pandis, S. N.: Atmospheric chemistry and physics: from air pollution to climate change, John Wiley & Sons, ISBN 978-1-118-94740-1, 2016.

Shen, X., Sun, J., Ma, Q., Zhang, Y., Zhong, J., Yue, Y., Xia, C., Hu, X., Zhang, S., and Zhang, X.: Long-term trend of new particle formation events in the Yangtze River Delta, China and its influencing factors: 7-year dataset analysis, Sci. Total Environ., 807, 150783, https://doi.org/10.1016/j.scitotenv.2021.150783, 2022.

Stone, V., Miller, M. R., Clift, M. J., Elder, A., Mills, N. L., Møller, P., Schins, R. P., Vogel, U., Kreyling, W. G., Jensen, K. A., Kuhlbusch, T. A., Schwarze, P. E., Hoet, P., Pietroiusti, A., Vizcaya-Ruiz, A. D., Baeza-Squiban, A., Teixeira, J. P., Tran, C. L., and Cassee, F. R.: Nanomaterials Versus Ambient Ultrafine Particles: An Opportunity to Exchange Toxicology Knowledge, Environ. Health Persp., 125, 106002, https://doi.org/10.1289/EHP424, 2017.

Thamban, N. M., Lalchandani, V., Kumar, V., Mishra, S., Bhattu, D., Slowik, J. G., Prevot, A. S., Satish, R., Rastogi, N., and Tripathi, S. N.: Evolution of size and composition of fine particulate matter in the Delhi megacity during later winter, Atmos. Environ., 267, 118752, https://doi.org/10.1016/j.atmosenv.2021.118752, 2021.

Tost, H., Jöckel, P., Kerkweg, A., Sander, R., and Lelieveld, J.: Technical note: A new comprehensive SCAVenging submodel for global atmospheric chemistry modelling, Atmos. Chem. Phys., 6, 565–574, https://doi.org/10.5194/acp-6-565-2006, 2006.

Trechera, P., Garcia-Marlès, M., Liu, X., Reche, C., Pérez, N., Savadkoohi, M., Beddows, D., Salma, I., Vörösmarty, M., Casans, A., Casquero-Vera, J. A., Hueglin, C., Marchand, N., Chazeau, B., Gille, G., Kalkavouras, P., Mihalopoulos, N., Ondracek, J., Zikova, N., Niemi, J. V., Manninen, H. E., Green, D. C., Tremper, A. H., Norman, M., Vratolis, S., Eleftheriadis, K., Gómez-Moreno, F. J., Alonso-Blanco, E., Gerwig, H., Wiedensohler, A., Weinhold, K., Merkel, M., Bastian, S., Petit, J.-E., Favez, O., Crumeyrolle, S., Ferlay, N., Martins Dos Santos, S., Putaud, J.-P., Timonen, H., Lampilahti, J., Asbach, C., Wolf, C., Kaminski, H., Altug, H., Hoffmann, B., Rich, D. Q., Pandolfi, M., Harrison, R. M., Hopke, P. K., Petäjä, T., Alastuey, A., and Querol, X.: Phenomenology of ultrafine particle concentrations and size distribution across urban Europe, Environ. Int., 172, 107744, https://doi.org/10.1016/j.envint.2023.107744, 2023.

Tsimpidi, A. P., Karydis, V. A., Pozzer, A., Pandis, S. N., and Lelieveld, J.: ORACLE 2-D (v2.0): an efficient module to compute the volatility and oxygen content of organic aerosol with a global chemistry–climate model, Geosci. Model Dev., 11, 3369–3389, https://doi.org/10.5194/gmd-11-3369-2018, 2018.

Twomey, S.: The nuclei of natural cloud formation part II: The supersaturation in natural clouds and the variation of cloud droplet concentration, Geofisica Pura e Applicata, 43, 243–249, https://doi.org/10.1007/BF01993560, 1959.

Villa, T., Jayaratne, E., Gonzalez, L., and Morawska, L.: Determination of the vertical profile of particle number concentration adjacent to a motorway using an unmanned aerial vehicle, Environ. Pollut., 230, 134–142, https://doi.org/10.1016/j.envpol.2017.06.033, 2017.

Wang, J., Krejci, R., Giangrande, S., Kuang, C., Barbosa, H. M. J., Brito, J., Carbone, S., Chi, X., Comstock, J., Ditas, F., Lavric, J., Manninen, H. E., Mei, F., Moran-Zuloaga, D., Pöhlker, C., Pöhlker, M. L., Saturno, J., Schmid, B., Souza, R. A. F., Springston, S. R., Tomlinson, J. M., Toto, T., Walter, D., Wimmer, D., Smith, J. N., Kulmala, M., Machado, L. A. T., Artaxo, P., Andreae, M. O., Petäjä, T., and Martin, S. T.: Amazon boundary layer aerosol concentration sustained by vertical transport during rainfall, Nature, 539, 416–419, https://doi.org/10.1038/nature19819, 2016.

Weigel, R., Mahnke, C., Baumgartner, M., Dragoneas, A., Vogel, B., Ploeger, F., Viciani, S., D'Amato, F., Bucci, S., Legras, B., Luo, B., and Borrmann, S.: In situ observation of new particle formation (NPF) in the tropical tropopause layer of the 2017 Asian monsoon anticyclone – Part 1: Summary of

StratoClim results, Atmos. Chem. Phys., 21, 11689–11722, https://doi.org/10.5194/acp-21-11689-2021, 2021.

WHO (World Health Organization): WHO Air quality guidelines for particulate matter, ozone, nitrogen dioxide and sulfur dioxide: global update 2005: summary of risk assessment, World Health Organization, Occupational and Environmental Health Team, https://www.who.int/publications/i/item/WHO-SDE-PHE-OEH-06-02 (last access: 17 February 2023), 2006.

Williamson, C. J., Kupc, A., Axisa, D., Bilsback, K. R., Bui, T., Campuzano-Jost, P., Dollner, M., Froyd, K. D., Hodshire, A. L., Jimenez, J. L., Kodros, J. K., Luo, G., Murphy, D. M., Nault, B. A., Ray, E. A., Weinzierl, B., Wilson, J. C., Yu, F., Yu, P., Pierce, J. R., and Brock, C. A.: A large source of cloud condensation nuclei from new particle formation in the tropics, Nature, 574, 399–403, https://doi.org/10.1038/s41586-019-1638-9, 2019.

Wu, T. and Boor, B. E.: Urban aerosol size distributions: a global perspective, Atmos. Chem. Phys., 21, 8883–8914, https://doi.org/10.5194/acp-21-8883-2021, 2021.

Wu, Z., Hu, M., Lin, P., Liu, S., Wehner, B., and Wiedensohler, A.: Particle number size distribution in the urban atmosphere of Beijing, China, Atmos. Environ., 42, 7967–7980, https://doi.org/10.1016/j.atmosenv.2008.06.022, 2008.

Zeng, Y., Cao, Y., Qiao, X., Seyler, B. C., and Tang, Y.: Air pollution reduction in China: Recent success but great challenge for the future, Sci. Total Environ., 663, 329–337, https://doi.org/10.1016/j.scitotenv.2019.01.262, 2019.

Zhao, B., Shrivastava, M., Donahue, N. M., Gordon, H., Schervish, M., Shilling, J. E., Zaveri, R. A., Wang, J., Andreae, M. O., Zhao, C., Gaudet, B., Liu, Y., Fan, J., and Fast, J. D.: High concentration of ultrafine particles in the Amazon free troposphere produced by organic new particle formation, P. Natl. Acad. Sci. USA, 117, 25344–25351, https://doi.org/10.1073/pnas.2006716117, 2020.